AGN Host Galaxies

Sylvain Veilleux

University of Maryland

Abstract

In this series of four lectures, I discuss four important aspects of AGN host galaxies. In Lecture #1, I address the starburst-AGN connection. First, I briefly review the primary diagnostic tools that are used to quantify and distinguish star formation and nuclear activity. Next I describe the best evidence for a connection between these two processes, first at low luminosity and then at high luminosity. In the last section, I summarize the main results and offer possible explanations. In Lecture #2, I discuss our current understanding of ultraluminous infrared galaxies ($\log[L_{IR}/L_{\odot}] \geq 12$; ULIRGs). First, I describe the general properties of ULIRGs, comparing the local sample with their distant counterparts. Then I discuss the role of ULIRGs in the formation and evolution of spheroids and their massive black holes. The discussion of their possible role in the metal enrichment of the IGM through superwinds is postponed until Lecture #3. In this third lecture, I discuss the importance of feedback processes in the local and distant universe. The emphasis is on mechanical feedback. I describe the basic physics of winds, a few classic examples of winds in the local universe, the statistical properties of winds, near and far, and their impact on galaxy formation and evolution. A list of potential thesis projects is given at the end. The fourth and final lecture is on elemental abundances as tracers of star formation. First, I explain the basic principles behind chemical evolution, and describe three simple models whose predictions are compared with observations in the Milky Way. Next I discuss and give an interpretation of the results of abundance determinations in local quiescent and starburst galaxies before discussing elemental abundances in the more distant universe.

Key words:
Galaxies: Abundances, Galaxies: Evolution, Galaxies: Formation, Galaxies: Interactions, Galaxies: Starburst, Galaxies: Quasars

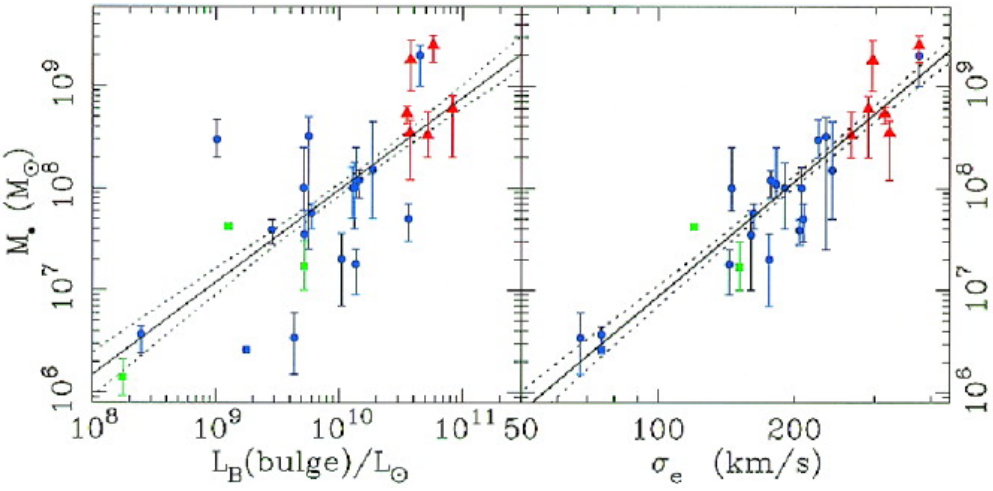

Fig. 1. Black hole mass versus bulge luminosity (left) and the luminosity-weighted aperture dispersion within the effective radius (right). Green squares denote galaxies with maser detections, red triangles are from gas kinematics, and blue circles are from stellar kinematics. Solid and dotted lines are the best-fit correlations and their 68% confidence bands. (From Gebhardt et al. 2000)

1 The Starburst-AGN Connection

1.1 Introduction

The apparent connection between black hole driven nuclear activity and starburst activity on large scale has been the topic of debates for many years (e.g., see references in review by Veilleux 2001). More than ever, this topic is relevant to help us understand galaxy formation and evolution, the global star formation and metal enrichment history of the universe, and the origin of nuclear activity and associated black hole growth.

The existence of an apparently tight relation (Fig. 1) between black hole masses and spheroid masses (or velocity dispersions; Gebhardt et al. 2000; Ferrarese & Merritt 2000) points to a causal connection between spheroid formation (via a starburst) and black hole growth (via nuclear activity). A flurry of theoretical papers have tried to make sense of these results. In many scenarios, gas or radiation pressure from a starburst- and/or AGN-driven wind helps shut off the fuel supply to the black hole and terminate star formation in the surrounding galaxy (e.g., Murray, Quataert, & Thompson 2005). Regardless of the exact process involved in regulating the black hole and spheroid growths (this topic of negative feedback is covered in Lecture #3 of this series, §3), the correlation indicates that the starburst-AGN connection is alive and well and has had a cosmologically important impact on galaxy formation and evolution.

To better understand this connection, one first needs to discuss the diagnostic tools that are used to detect and distinguish star formation and nuclear activity. This is done in §1.2. In §1.3, I describe key results from recent studies of low- and high-luminosity AGNs. In §1.4, I summarize the results and offer a few possible explanations.

1.2 Star Formation Diagnostics

A very useful paper here is Kennicutt (1998). The material in §§1.2.1 – 1.2.4 is taken directly from that review and is therefore not described in detail.

1.2.1 Ultraviolet

Hot, young stars emit copious amounts of UV radiation (e.g., Leitherer et al. 1999). The strength of the UV (1500 – 2800 Å) continuum scales linearly with the luminosity of young stars and therefore with the star formation rate. For solar abundances and a Salpeter Initial Mass Function (≡ IMF, 0.1 – 100 $M_\odot$):

$$SFR(M_\odot \text{ yr}^{-1}) = 1.4 \times 10^{-28} L_\nu(\text{ergs s}^{-1}\text{Hz}^{-1})$$

1.2.2 Recombination Lines

Hot, young stars emit radiation that ionizes the surrounding ISM. The Strömgren sphere is the spherical volume of this HII region where the rate of ionizations balances the rate of recombinations. The nebular lines produced in the HII region effectively re-emit the integrated stellar luminosity shortward of the Lyman limit (*i.e.* ≥ 13.6 eV). The intensity of these lines scales linearly with the number of hot, young stars and therefore the star formation rate. For solar abundances and a Salpeter IMF (0.1 – 100 $M_\odot$):

$$SFR(M_\odot \text{ yr}^{-1}) = 7.9 \times 10^{-42} L_{H\alpha}(\text{ergs s}^{-1})$$

1.2.3 Forbidden Lines

Hα is redshifted out of the visible window beyond $z \sim 0.5$. In principle, Hβ and the higher order Balmer emission lines could be used to estimate star formation rates, but these lines are weak and stellar absorption more strongly influences their emission-line fluxes than that of Hα.

Neutral oxygen has the same ionization potential as hydrogen (13.6 eV). This means that ionized oxygen coexists with ionized hydrogen and therefore lines produced by ionized oxygen scales with the number of hot, young stars in HII regions. The strongest emission feature in the blue is the [O II] $\lambda\lambda$3726, 3729 forbidden-line doublet. The strength of these collisionally excited lines is sensitive to abundance and ionization state (electron temperature) of the gas, more so than the recombination lines. A rough calibration is:

$$SFR(M_\odot \text{ yr}^{-1}) = (1.4 \pm 0.4) \times 10^{-41} L_{[OII]}(\text{ergs s}^{-1})$$

Given its blue wavelength, this doublet is also more sensitive to dust extinction than Hα.

1.2.4 Far-Infrared Continuum

A significant fraction of the bolometric luminosity of a galaxy may be absorbed by interstellar dust and re-emitted in the thermal infrared (10 – 300 μm). The absorption cross-section of the dust is strongly peaked in the UV, so to first order the far-infrared emission scales with the star formation rate. In the limiting case of a dust cocoon surrounding a star-forming galaxy:

$$SFR(M_\odot \text{ yr}^{-1}) = 4.5 \times 10^{-44} L_{FIR}(\text{ergs s}^{-1})$$

1.2.5 AGN Contamination

In many cases (particularly at higher redshifts), it is difficult to spatially resolve the emission produced by star formation from that produced by the AGN. In this situation, one must use spectroscopic methods to disentangle the two processes. In some instance, one may use the strengths of stellar atmospheric features to quantify the starburst. These include the Balmer series, Ca I triplet $\lambda\lambda\lambda$8498, 8542, and 8662 in the visible/deep-red and Si IV λ1400, C IV λ1550, and He II λ1640 in the UV (Robert et al. 1993).

The emission lines produced in the ionized gas also bear the signature of the source of energy. The ionizing spectra of all but the hottest O stars cut off near the He II edge (54.4 eV), while AGNs are generally strong X-ray emitters. These high-energy photons have two effects on the emission line spectrum: (1) the material near the AGN is more highly ionized and emit strong high-ionization lines; (2) due to the strong energy dependence of the absorption cross-section ($\sigma_\nu \propto \nu^{-3}$), these high-energy photons are absorbed deeper into the gas clouds and produce extended partially ionized zones. These zones are

strong emitters of collisionally excited low-ionization lines. One therefore expects an enhancement of *both* high- and low-ionization lines in AGN relative to those in HII regions. Several diagnostic diagrams at optical and near-infrared wavelengths have been designed to specifically take advantage of these differences (e.g., Veilleux & Osterbrock 1987; Osterbrock, Tran, & Veilleux 1992; Kewley et al. 2001).

In deeply obscured galaxies, the UV, optical, and near-infrared diagnostics cannot be used to distinguish between starbursts and AGN. One must rely on the relative intensities of the mid-infrared fine structure lines and/or the strengths (equivalent widths) of the polycyclic aromatic hydrocarbon (PAH) features. The principles behind the use of the fine structure lines are roughly the same as for the optical/UV lines *i.e.* use line ratio diagrams that take advantage of the fact that AGN are copious emitters of low- and high-ionization lines. The use of the PAH features nicely complements that of the fine structure lines since they are generally easier to detect in the fainter, more distant galaxies. The PAH features are less visible in AGN due to the much stronger continuum in these objects and possible PAH destruction.

1.3 Evidence for a Starburst-AGN Connection

Since the triggering mechanism for AGN activity probably depends on the luminosity of the AGN, I make a distinction in the following discussion between the nearby, low-luminosity Seyferts and Fanaroff-Riley type I (FR I) radio galaxies and the more distant and powerful quasars, Fanaroff-Riley type II (FR II) radio galaxies, and ultraluminous infrared galaxies (ULIRGs; log $[L_{IR}/L_{\odot}]$ $\geq$ 12 by definition - this is the subject of Lecture #2; §2).

1.3.1 Low-Luminosity AGN

Direct evidence for recent nuclear star formation exists in a number of Seyfert 2 galaxies (*i.e.* Seyferts without broad recombination lines). Optical and ultraviolet spectroscopy of the nuclear regions of these galaxies often reveals the signatures of young and intermediate-age stars. The stellar Ca II triplet feature at $\lambda\lambda\lambda$8498, 8542, 8662 in Seyfert 2s has an equivalent width similar to that in normal galaxies while the stellar Mg Ib λ5175 is often weaker (Terlevich, Diaz, & Terlevich 1990; Cid Fernandes et al. 2004). This result is difficult to explain with a combination of an old stellar population and a featureless power-law continuum from an AGN. The most natural explanation is that young red supergiants contribute significantly to the continuum from the central regions.

Evidence for intermediate-age (a few 100 Myrs) stars in Seyfert galaxies is

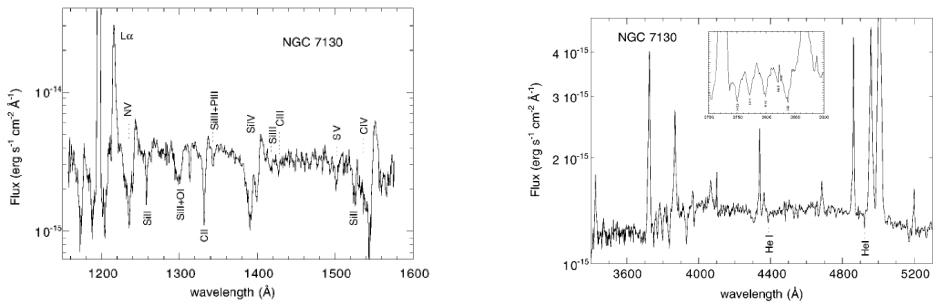

Fig. 2. (*left*) UV spectrum of NGC 7130. It is displayed in log (F_λ) to show the emission and absorption lines. The most important stellar wind and photospheric absorption lines are labeled. (*right*) Normalized optical spectrum of NGC 7130 (dashed line) plotted with the normalized spectrum of a B0 V star combined with a G0 V star (thick line). 60% of the light is from a B0 V and 40% from a G0 V star. The comparison shows that most of the stellar features in NGC 7130 are well reproduced by a combination of young (B0 V) and old (G0 V) stars. (From Gonzalez Delgado et al. 1998)

also apparent in the blue part of the spectrum, where the high-order Balmer series and He I absorption lines appear to be present in more than half of the brightest Seyfert 2 galaxies (e.g., Cid Fernandes & Terlevich 1995; Joguet et al. 2001; González Delgado, Heckman, & Leitherer 2001; Fig. 2). A few of these objects may even harbor a broad emission feature near 4680 Å, possibly the signature of a population of young (a few Myrs) Wolf-Rayet stars (González Delgado et al. 2001). The ultraviolet continuum from some of the brightest UV Seyfert 2s also appears to be dominated by young stars based on the strength of absorption features typically formed in the photospheres and in the stellar winds of massive stars (e.g., Heckman et al. 1997; González Delgado et al. 1998; Fig. 2). The bolometric luminosities of these nuclear starbursts ($\sim 10^{10}$ $L_\odot$) are similar to the estimated bolometric luminosities of their obscured Seyfert 1 nuclei. This explains why UV-bright stellar clusters are more frequently detected in Seyfert 2s than in Seyfert 1s (Muñoz Marín et al. 2007). The recent detection of near-infrared CN bands in Seyferts brings support to the idea that star formation is indeed connected to the AGN in these objects (Riffel et al. 2007).

In recent years, SDSS has contributed significantly to our knowledge of local AGNs. For instance, Kauffmann et al. (2003b) have studied a sample of 22,623 narrow-line AGN with $0.02 < z < 0.3$. They find that the hosts of low-luminosity AGN have a stellar population similar to that of normal early-type galaxies, while the hosts of high-luminosity AGN have much younger mean stellar ages. Indeed, young (< 1 Gyr) stellar population appears to be a general property of AGN with high [O III] luminosity (Figs. 3 and 4). This is true regardless of the presence of broad recombination lines (*i.e.* types 1 and 2). The young stars are spread out over scales of at least a few kpc.

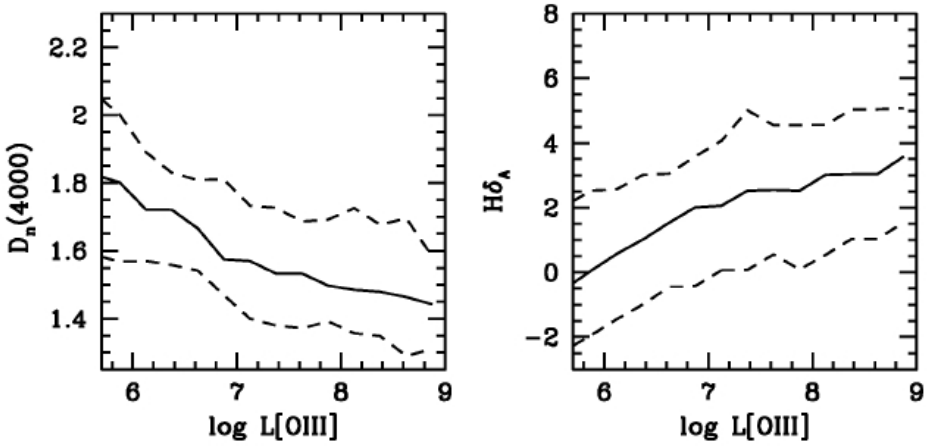

Fig. 3. The strengths of the 4000 Å break and Hδ absorption feature are plotted as a function of log $L[O\ III]$. The solid line shows the median, while the dashed lines indicate the 16-84 percentiles of the $1/V_{max}$ weighted distribution. (From Kauffmann et al. 2003b)

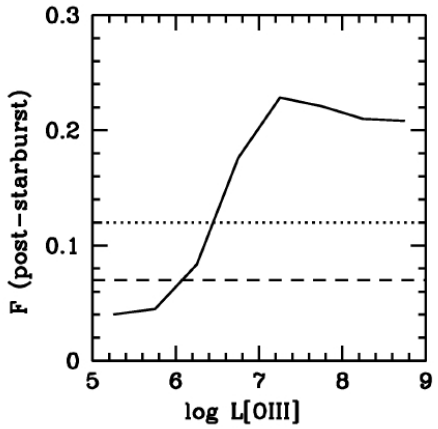

Fig. 4. The fraction F of AGN with Hδ_A values that are displaced by more than 3 σ above the local of star-forming galaxies is plotted as a function of log $L[O\ III]$. The dashed line indicates the fraction of such systems in the subsample of normal massive galaxies. The dotted line indicates the fraction of such systems in the subsample of normal massive galaxies with $D_n(4000) < 1.6$. (From Kauffmann et al. 2003b)

1.3.2 High-Luminosity AGN

Abundant molecular gas has been detected in radio galaxies and quasars (e.g., Evans et al. 2001), but is this gas forming stars? The extensive multiwavelength data set on these objects seems to indicate that starbursts are indeed present in local and distant quasars. Approximately 20 – 30% of all PG QSOs show an infrared excess $L_{IR}/L_{blue} > 0.4$. IR-excess QSOs tend to have large dust and H_2 masses, suggesting that the infrared – submm "bump" in the spectral energy distribution of PG QSOs is due to star formation.

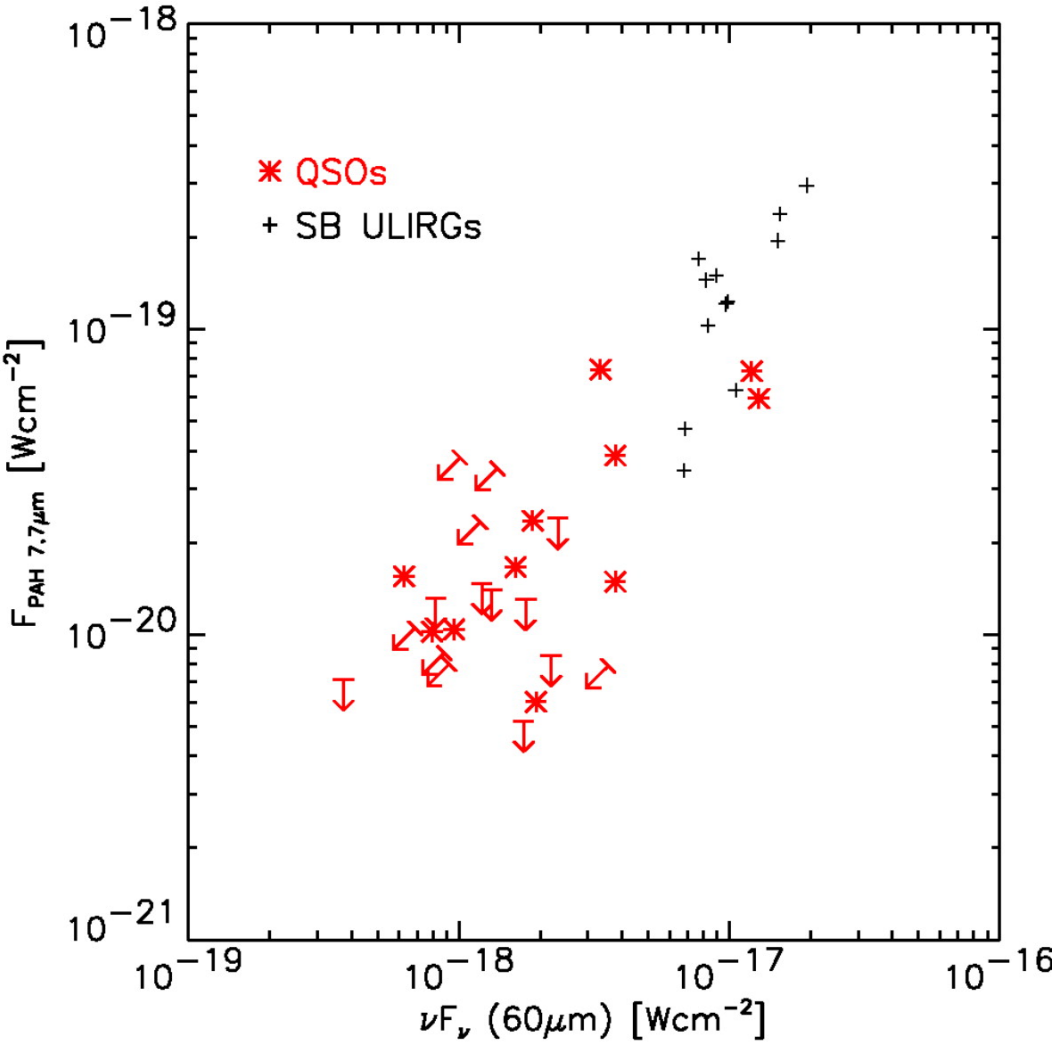

Fig. 5. PAH fluxes F(PAH 7.7 μ) vs. F(60 μm) for local QSOs and starburst-dominated ULIRGs. (From Schweitzer et al. 2006)

More direct evidence for a starburst-AGN connection has recently been found in local quasars from Spitzer mid-infrared spectroscopy (Schweitzer et al. 2006; Shi et al. 2007). PAH emission is detected in 11 of 26 PG QSOs and in the average spectrum of the other 15 PG QSOs (Schweitzer et al. 2006). The strength of the PAHs in these quasars is consistent with the far-infrared luminosity being produced primarily by U/LIRG-like starbursts with star formation rates of order 2 – 300 $M_\odot$ yr^{-1} (Fig. 5). The strength of the starburst (measured by the FIR or PAH luminosity) correlates with that of the QSO (based on the 5100 Å luminosity, a direct indicator of the mass accretion rate onto the black hole; Netzer et al. 2007; Fig. 6). This suggests a strong starburst – AGN connection in these objects.

A recent Spitzer study of high-z quasars by Maiolino et al. (2007a) fail to detect PAH emission in these objects. This would indicate that the correlation

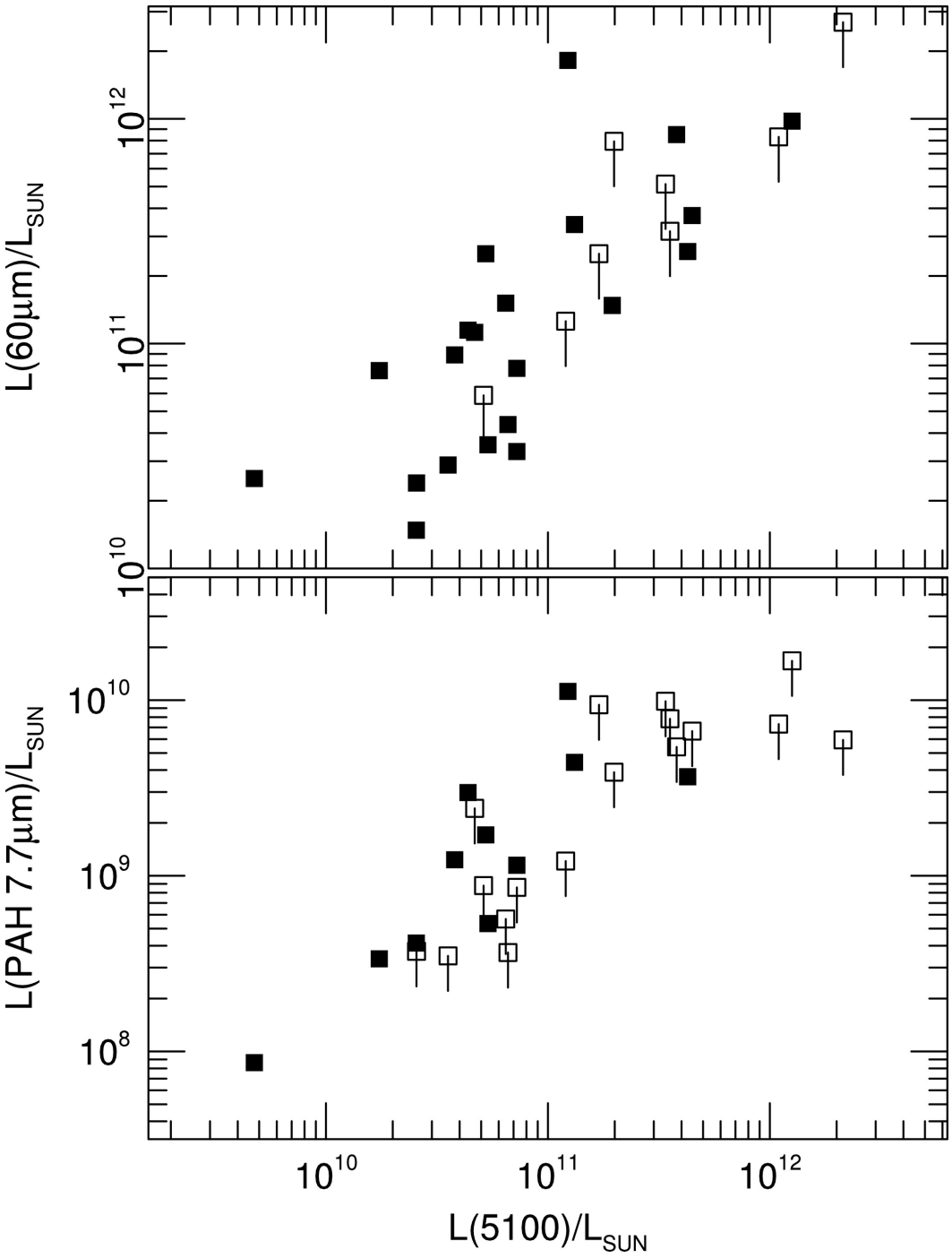

Fig. 6. *Top* : Correlation of the optical (5100 Å) and FIR (60 μm) continuum luminosities. *Bottom* : L(5100) vs. L(PAH 7.7 μm) showing detections (filled squares) and upper limits (open squares). (From Netzer et al. (2007)

between star formation rate and AGN power "saturates" at high luminosities (Fig. 7). The "flattening" of the relation also seems to be present for CO emission (Maiolino et al. 2007b). It may therefore be that not enough fuel is available at high z to fuel the starburst and match the strength of the AGN

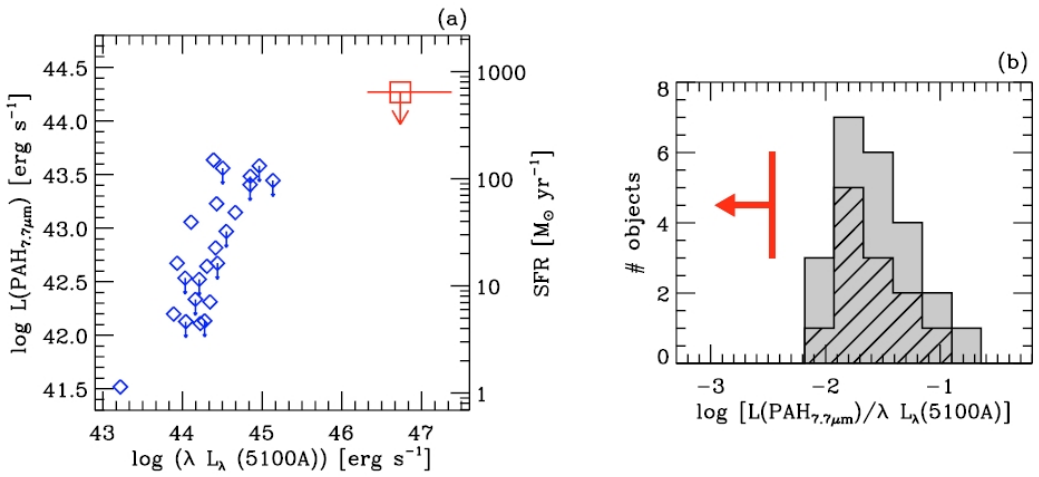

Fig. 7. (*a*) PAH(7.7 μm) luminosity as a function of the QSO optical luminosity. Blue diamonds are data from Schweitzer et al. (2006). The red square is the upper limit obtained by the average spectrum of luminous, high-z QSOs. (*b*) Distribution of the PAH(7.7 μm) to optical luminosity ratio in the local QSOs sample of Schweitzer et al. (2006). The hatched region indicates upper limits. The red vertical line indicate the upper limit inferred from the average spectrum of luminous QSOs at high-z. (From Maiolino et al. 2007a)

in these quasars.

1.4 Discussion

As explained in §1.3, starbursts often coexist with actively accreting supermassive black holes, but the starburst-AGN relation appears to be tighter at high luminosity than at low luminosity. This suggests that black hole fueling in low-luminosity AGN is more stochastic and does not necessarily scale with the surrounding starburst.

The fueling of AGN requires mass accretion rates $\dot{M} \approx 1.7\ (0.1\ /\ \epsilon)(\mathrm{L}/10^{46}$ ergs $\mathrm{s}^{-1})\ \mathrm{M}_{\odot}\ \mathrm{yr}^{-1}$, where ϵ is the mass-to-energy conversion efficiency. A modest accretion rate of order $\sim 0.01\ \mathrm{M}_{\odot}\ \mathrm{yr}^{-1}$ is therefore sufficient to power a Seyfert galaxy. Only a small fraction of the total gas content of a typical host galaxy is therefore necessary for the fueling of these low-luminosity AGNs. A broad range of mechanisms including intrinsic processes (e.g., stellar winds and collisions, dynamical friction of giant molecular clouds against stars; nuclear bars or spirals produced by gravitational instabilities in the disk) and external processes (e.g., minor galaxy interaction or mergers) may be at work in these objects. So it may not be surprising after all that the power of these AGN does not necessarily scale with the surrounding starburst.

The stringent requirements on the mass accretion rates for luminous AGNs almost certainly require external processes such as major galaxy interactions or mergers to be involved in triggering and sustaining this high level of activity over $\sim 10^8$ years. Starbursts are a natural consequence of major mergers. This topic will be discussed in more detail in Lecture #2 (§2). A lack of "fuel" (= molecular gas) may explain the apparent break in the starburst-AGN correlation at very high AGN luminosities.

2 Ultraluminous Infrared Galaxies

2.1 Introduction

In this lecture, I adopt the following standard definitions:

- Luminous infrared galaxies (≡ LIRGs) have $\log[L_{IR}/L_\odot] \geq 11.0$.
- Ultraluminous infrared galaxies (≡ ULIRGs) have $\log[L_{IR}/L_\odot] \geq 12.0$,

where the infrared luminosity $L_{IR} \equiv L(8 - 1000\ \mu m)$. The focus of this lecture is the ULIRGs, although we also discuss LIRGs when relevant to our understanding of ULIRGs. The literature on ULIRGs has been reviewed in a number of excellent articles: Sanders & Mirabel (1996), Blain et al. (2002), and Lonsdale, Farrah, & Smith (2006). These last two articles emphasize the important role that new instrumentation [particularly SCUBA on the James Clerk Maxwell Telescope (JCMT) and IRAC, MIPS, and IRS on the Spitzer Space Telescope (SST)] has played in the discovery and follow-up study of the ever-expanding population of distant ULIRGs. This short lecture attempts to encapsulate the most important aspects of these objects. For more information, the readers are advised to consult these three reviews and the original papers listed in the text.

In §2.2, I describe the key properties of ULIRGs, both near and far. Next (§2.3), I discuss the role that ULIRGs appears to play in the formation and evolution of spheroids and their massive black holes. ULIRGs may also contribute to the metal enrichment of the IGM through superwinds, but the discussion of this important aspect of ULIRGs is postponed until Lecture #3 of this series (§3).

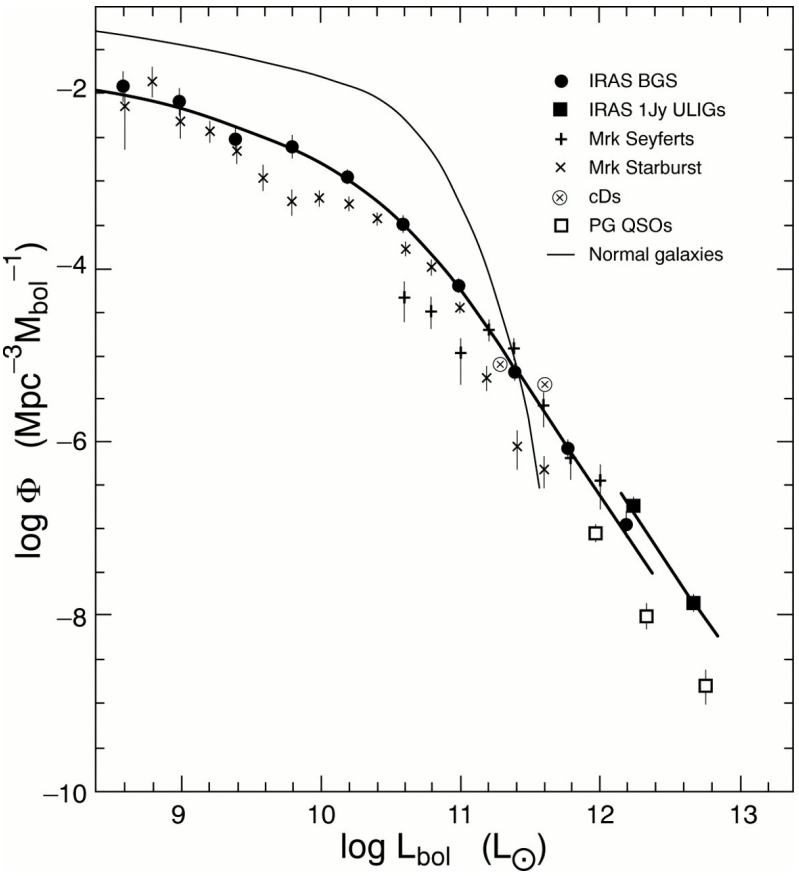

Fig. 8. The luminosity function for infrared galaxies compared with other extragalactic objects. (From Sanders & Mirabel 1996)

2.2 Properties of ULIRGs: Near & Far

2.2.1 Luminosity Function

LIRGs and ULIRGs are the dominant extragalactic population in the local universe at $L_{BOL} > 10^{11}$ L$_\odot$ (Fig. 8). On average, ~ 0.008 ULIRG at $z < 0.2$ is found within each square degree on the sky. Their number density is $\sim 2.5 \times 10^{-7}$ Mpc^{-3}. The luminosity function at these high luminosities is best described by a power law with a slope of $\sim$ –2.35. Overall, ULIRGs are more numerous than optical selected QSOs, although results from new optical and infrared surveys have recently brought the number of known QSOs up closer to that of ULIRGs (e.g., Wisotzki 2000).

2.2.2 Spectral Energy Distribution

The spectral energy distribution of ULIRGs is dominated by a large mid-to-far infrared bump: more than $\sim 80\%$ of the bolometric luminosity of ULIRGs is emitted in this wavelength region (Fig. 9; Sanders & Mirabel 1996). This

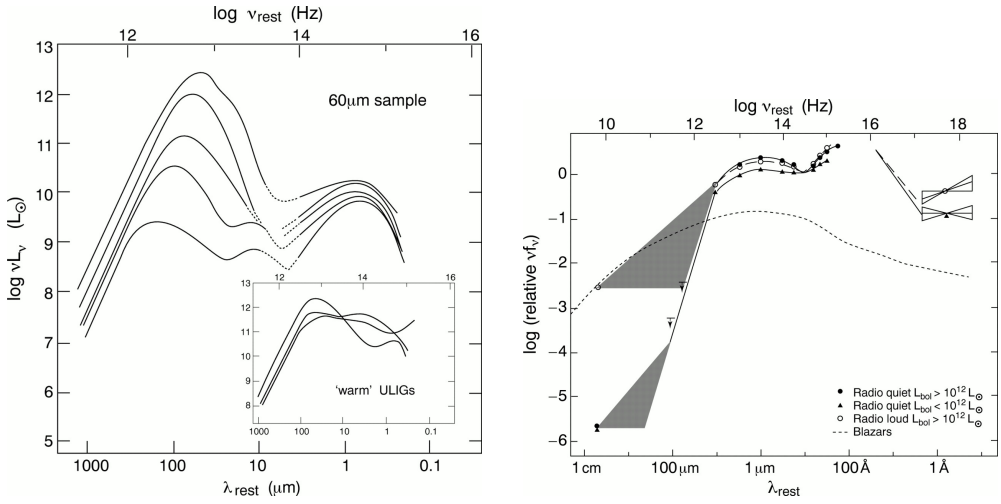

Fig. 9. (*left*) Variation of the mean SEDs (from submillimeter to UV wavelengths) with increasing $L_{\rm IR}$ for a 60 μm sample of infrared galaxies. (Insert) Examples of the subset (15%) of ULIRGs with "warm" infrared color ($f_{25}/f_{60} > 0.3$). (*right*) Mean spectral energy distributions from radio to X-ray wavelengths of optically selected radio-loud and radio-quiet QSOs and blazars. (From Sanders & Mirabel 1996)

emission is due to warm (30 – 200 K) dust heated by a starburst and/or an AGN. A significant ($\sim$ 15%) subset of all local ULIRGs have "warm" mid-infrared colors ($f_{25}/f_{60} > 0.2$), more typical of powerful radio galaxies and optically selected quasars. A direct comparison of the SEDs of warm ULIRGs with those of PG QSOs emphasizes the resemblance (Fig. 9). The mean SED of optical selected QSOs is dominated by the "big blue bump" ($\sim$ 0.05 – 0.5 μm) and thermal emission from an infrared/submillimeter bump ($\sim$ 1 – 300 μm), which is typically 30% as strong as the big blue bump. About 20 – 30% of all PG QSOs have an infrared excess $L_{IR}/L_{BBB} > 0.4$. This resemblance in SEDs has been used to argue that warm ULIRGs represent transition objects between cool ULIRGs and QSOs (e.g., Sanders et al. 1988a,b). We return to this point in §2.3.

2.2.3 Evolution

Results from several studies with the Infrared Space Observatory (ISO), Spitzer Space Telescope (SST), and SCUBA on the JCMT have revealed a strong evolution in the luminosity function at the highest infrared luminosities (which was hinted by the earlier *IRAS* data). For instance the number density of submm galaxies (SMGs) discovered with SCUBA at $z \sim 2$ is 10^{2-3} times the number density of local ULIRGs, *i. e.* similar to the number density of bright QSOs at $z \sim 2$ (Chapman et al. 2005). This luminosity dependence of the evolution has been confirmed with SST (Perez-Gonzalez et al. 2005; Fig. 10). LIRGs and ULIRGs become important contributors to the extragalactic infrared background at $z \sim 1$ and $z \sim 2$, respectively (Le Floc'h et al. 2005;

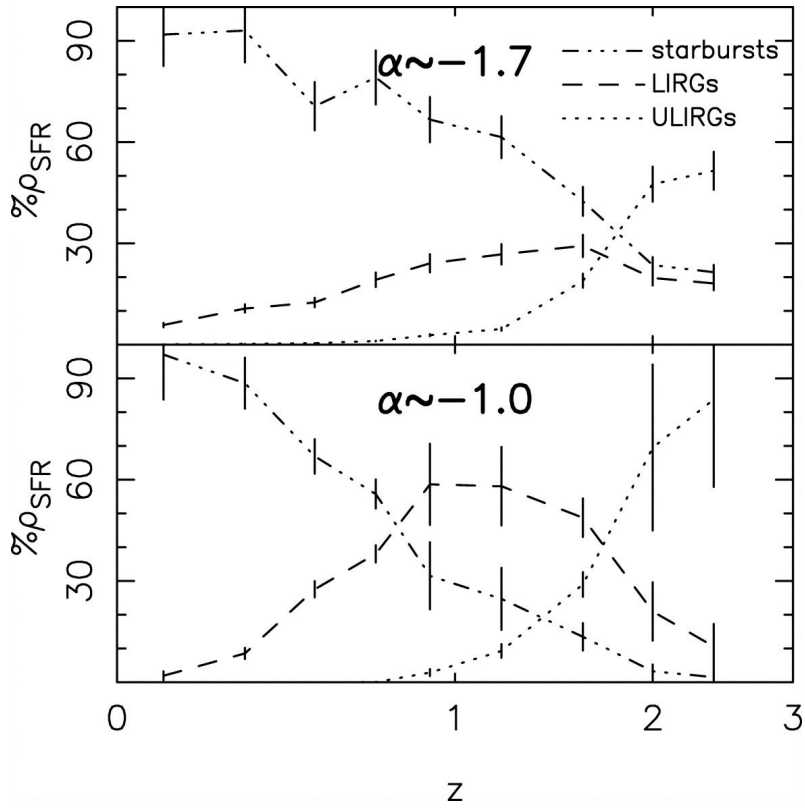

Fig. 10. Relative contribution of starbursts ($L_{\rm IR} < 10^{11}$ $L_\odot$), LIRGs ($L_{\rm IR} > 10^{11}$ $L_\odot$), and ULIRGs ($L_{\rm IR} > 10^{12}$ $L_\odot$) to the total SFR density of the universe as a function of redshift. Top and bottom panels show the two extreme cases of the faint-end slope value. The error bars show the uncertainties on the integration in each luminosity range, considering the errors of the individual luminosity function parameters. (From Perez-Gonzalez et al. 2005)

Fig. 11).

2.2.4 Morphology

All but one object in a local sample of 118 ULIRGs show signs of a strong tidal interaction/merger (Veilleux, Kim, & Sanders 2002). Multiple mergers involving more than two galaxies are seen in less than 5% of these systems. None of the local ULIRGs is in the first-approach stage of the interaction, and most (56%) of them harbor a single disturbed nucleus and are therefore in the later stages of a merger (Fig. 12). The fraction of post/old mergers (*i. e.* single-nucleus systems) increases with infrared luminosity. This trend with luminosity is seen within the class of ULIRGs but is even more obvious when combining LIRGs with ULIRGs (Ishida 2004; Veilleux et al. 2002): this fraction is $\sim$ 10% (20%) among LIRGs with $\log[L_{IR}/L_\odot] = 11.25 - 11.50$ (11.5 - 11.75), increases to $\sim$ 50% among ULIRGs with $\log[L_{IR}/L_\odot] = 12.0 - 12.2$, and peaks at $\sim$ 80% among the most luminous ($\log[L_{IR}/L_\odot] > 12.5$) ULIRGs.

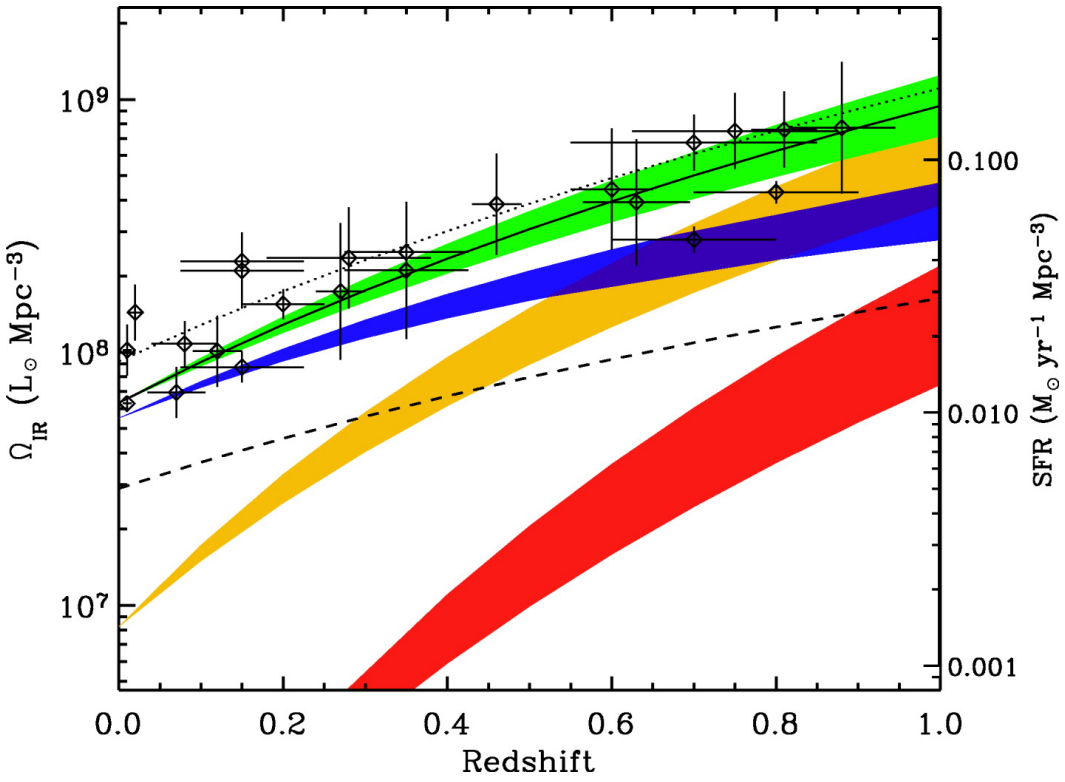

Fig. 11. Evolution of the comoving IR energy density up to $z \sim 1$ (green filled region) and the respective contributions from low-luminosity galaxies (*i.e.*, $L_{\rm IR} < 10^{11}$ L$_\odot$; blue filled area), IR-luminous sources (*i.e.*, $L_{\rm IR} > 10^{11}$ L$_\odot$; orange filled region), and ULIRGs (*i.e.*, $L_{\rm IR} > 10^{12}$ L$_\odot$; red filled region). The solid line evolves as $(1+z)^{3.9}$ and represents the best fit of the total IR luminosity density at $0 \leq z \leq 1$. Estimates are translated into an IR-equivalent SFR density given on the right vertical axis, where an absolute additional uncertainty of 0.3 dex should be added to reflect the dispersion in the conversion between luminosities and SFR. Note that the percentage of the contribution from each population is likely independent of this conversion. The dashed line corresponds to the SFR measured from the UV luminosity not corrected from dust extinction. The dotted line represents the best estimate of the total SFR density as the sum of this uncorrected UV contribution and the best fit of the IR-SFR (solid line). At $z \sim 1$ IR-luminous galaxies represent 70% $\pm$ 15% of the comoving IR energy density and dominate the star formation activity. Open diamonds and vertical and horizontal bars represent integrated SFR densities and their uncertainties estimated within various redshift bins and taken from the literature. (From Le Floc'h et al. 2005)

Distant ULIRGs also often appear to be undergoing a merger. Most high-z SMGs (50 – 60% at optical wavelengths and 85% in the UV) are multi-component or disturbed systems, suggestive of mergers or interactions (e.g., Chapman et al. 2003; Smail et al. 2004).

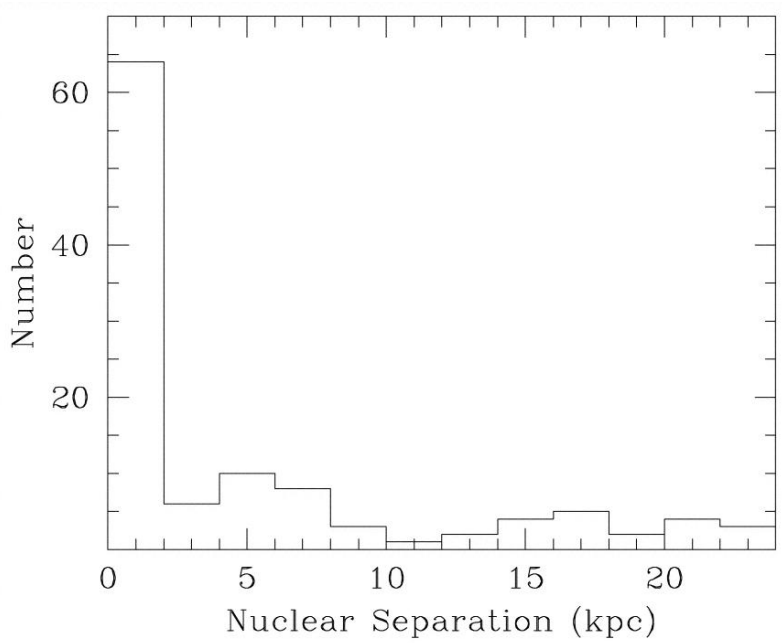

Fig. 12. Apparent nuclear separations in the 1-Jy sample of galaxies. The distribution is highly peaked at small values but also presents a significant tail at high values. The very uncertain separation measured in F11223−1244 (87.9 kpc) is not shown in this figure. (From Veilleux et al. 2002)

2.2.5 Gas Content

ULIRGs are extremely rich in molecular gas with H_2 masses of a few $\times$ 10^{10} $M_\odot$, more than an order of magnitude that of the Milky Way galaxy (e.g., Sanders et al. 1988c). The physical conditions in this gas are similar to those in massive giant molecular cloud (GMC) cores in our own Galaxy, although they are slightly more infrared luminous per unit of molecular gas mass and denser than GMC cores (Solomon et al. 1997). Remarkably about 40 – 10% of this molecular gas lies within the central kpc of ULIRGs. This implies molecular gas surface densities of $\sim$ few $\times$ 10^4 $M_\odot$ pc^{-2}, similar to the stellar densities of the core of elliptical galaxies (e.g., Downes & Solomon 1998). This large concentration of activity in ULIRGs is also seen at mid-infrared wavelengths (Soifer et al. 2000). These results are a natural consequence of merger-induced activity: in modern simulations of galaxy mergers the gas originally distributed over the entire body of each galaxy is funnelled rapidly to the central kpc of the merger due to bar-induced torques and energy dissipation, triggering a powerful nuclear starburst and possibly fueling an AGN (e.g., Barnes & Hernquist 1996; Mihos & Hernquist 1996; Hopkins et al 2006).

2.3 Importance of ULIRGs

2.3.1 Spheroids in Formation

The end-result of the simulations discussed in §2.2.5 is an elliptical-like merger remnant, but do observations support this picture? To answer this question careful imaging and spectroscopic studies of ULIRG are needed to derive the morphology and kinematics of the underlying host galaxies, and compare the results with those of normal ellipticals. In Veilleux et al. (2006), we found that the removal of the central PSF emission associated with the AGN or nuclear starburst is an important source of errors in the analysis of the surface brightness profiles in the more nucleated ULIRGs (*i. e.* those in the later stage of a merger). A detailed two-dimensional analysis of the surface brightness distributions in these objects indicates that the great majority (81%) of the single-nucleus systems show a prominent early-type morphology. As shown in Fig. 13, the hosts of ULIRGs lie close to the locations of intermediate-size ($\sim 1 - 2\ L^*$) spheroids in the photometric projection of the fundamental plane of ellipticals, although there is a tendency for the ULIRGs with small hosts to be brighter than normal spheroids. Excess emission from a merger-triggered burst of star formation in the ULIRG hosts may be at the origin of this difference.

VLT/Keck near-infrared stellar absorption spectroscopy has also been carried out to constrain the host dynamical mass for many of these ULIRGs. The analysis of these data (Dasyra et al. 2006ab) builds on the analyses of Genzel et al. (2001) and Tacconi et al. (2002) and reveals that the majority of ULIRGs are triggered by almost equal-mass major mergers of 1.5:1 average ratio, in general agreement with Veilleux et al. (2002). In Dasyra et al., we also find (see Fig. 14) that coalesced ULIRGs resemble intermediate mass ellipticals/lenticulars with moderate rotation, in their velocity dispersion distribution, their location in the fundamental plane (FP; e.g., Kormendy & Djorgovski 1989) and their distribution of the ratio of rotation/velocity dispersion [$\mathrm{v_{rot}}$ sin(i)/σ]. These results therefore suggest that ULIRGs form moderate mass ($m^* \sim 10^{11}$ $\mathrm{M_\odot}$), but not giant ($5 - 10 \times 10^{11}$ $\mathrm{M_\odot}$) ellipticals. These results are largely consistent with those from our imaging studies.

A similar analysis of the distant ULIRGs is obviously much more difficult. Current results suggest that high-z submm galaxies are on average bigger and more gas-rich systems than local ULIRGs (see Table 1 for a head-to-head comparison). The activity in these objects appears to be more extended than in local ULIRGs, so the high-z ULIRGs may not be simply scaled-up versions of local ULIRGs (Chapman et al. 2003).

A simple exercise in "numerology" quickly shows that local ULIRGs cannot be an important contributors of early-type galaxies: the number density of

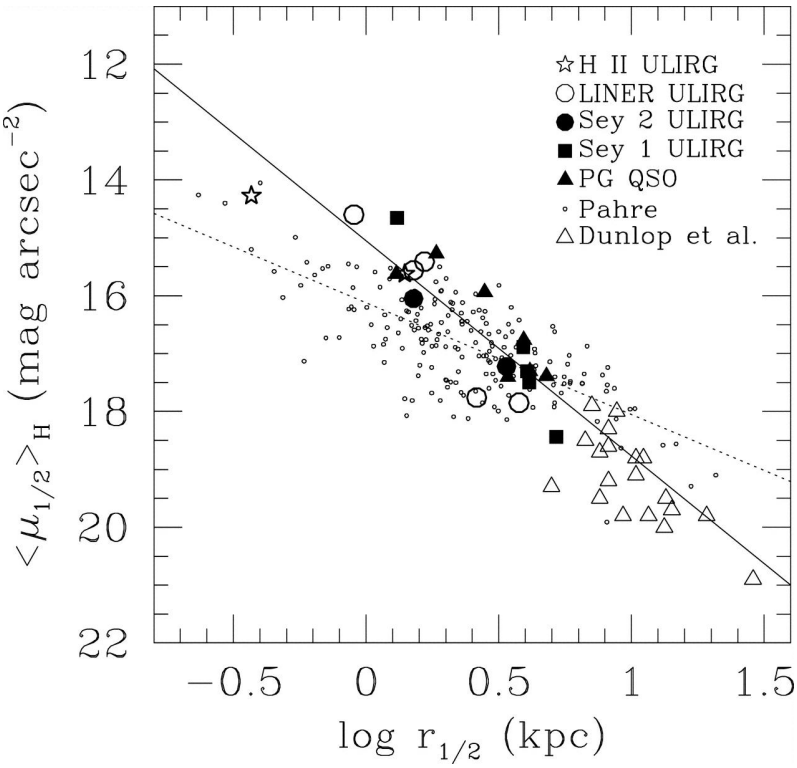

Fig. 13. Surface brightnesses vs. half-light radii for the early-type host galaxies in the sample of Veilleux et al. (2006). The hosts of the seven PG QSOs in the sample are statistically indistinguishable from the hosts of the 1 Jy ULIRGs. Both classes of objects fall near the photometric fundamental plane relation of elliptical galaxies as traced by the data of Pahre (1999; dashed line), although the smaller objects in our sample tend to lie above this relation (the solid line is a linear fit through our data points). This may be due to excess H-band emission from a young stellar population. ULIRGs and PG QSOs populate the region of the photometric fundamental plane of intermediate-size ($\sim 1-2$ L*) elliptical/lenticular galaxies. In contrast, the hosts of the radio-bright quasars of Dunlop et al. (2003) are massive elliptical galaxies that are significantly larger than the hosts of ULIRGs and PG QSOs. For this comparison, the R-band half-light radii tabulated in Dunlop et al. were taken at face value, and the surface brightnesses in that paper were shifted assuming $R - H = 2.9$, which is typical for early-type systems at $z \sim 0.2$. (See Veilleux et al. 2006 for more detail)

local ULIRGs $\sim 2.5 \times 10^{-7}$ Mpc^{-3} $\sim$ (1/7000) $\times$ number density of SDSS ellipticals. The story at high redshifts is different. The current best estimates for the stellar masses and dynamical masses in the cores of high-z ULIRGs are $\sim 10^{11}$ M$_\odot$. The ULIRG lifetime of these objects, estimated from stellar population analyses, is $\sim 200-300$ Myr, *i.e.* of the same order of magnitude as the gas consumption time scale (~ 40 Myr). The ULIRG era spans $z \sim 1.5-3$, corresponding to a time scale of ~ 1.5 Gyr (this number is quite uncertain; here we have choosen a conservatively low number). So the expected number density of descendants from these high-z ULIRGs is n(descendants) = n(bright

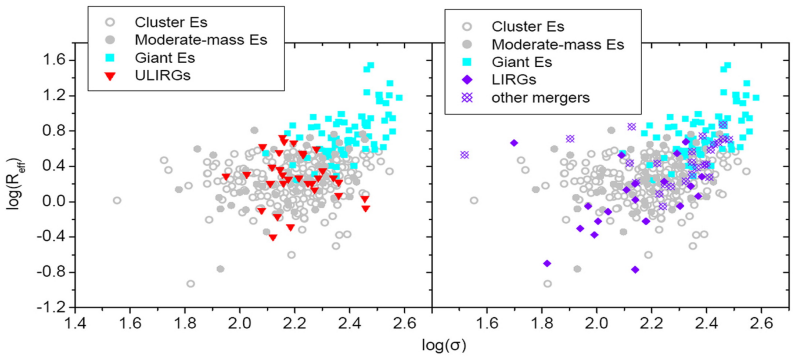

Fig. 14. R_{eff} - σ projection of the early-type galaxy FP. For viewing clarity, the various types of mergers are plotted in separate panels. The ULIRG remnants are plotted as triangles (left panel). The LIRGs and other (visually selected) mergers are plotted as diamonds and open-crossed diamonds, respectively (right panel). The effective radii of all merger remnants used in this figure are equal to the averages of their NIR measurements, if more than one is available. (See Dasyra et al. 2006b for more detail)

Table 1. Comparison of Distant Submm Galaxies with Local ULIRGs

Property	Submm Galaxies	Local ULIRGs
$< v_c >$	400 km s^{-1}	240 km s^{-1}
$< M_{dyn,1/2} >$	7×10^{10} M$_\odot$	5×10^{9} M$_\odot$
$< R_{1/2} >$	2.0 kpc	0.6 kpc
$< L_{BOL} >$	$10^{13.1}$ L$_\odot$	$10^{12.2}$ L$_\odot$
$< M_{gas}/M_{dyn} >$	0.3 – 0.4	0.16
$< \Sigma_{dyn} >$	5000 M$_\odot$ pc^{-2}	4900 M$_\odot$ pc^{-2}

SMGs) $\times$ [τ(ULIRG era) / τ(ULIRG lifetime)] $\sim 3 \times 10^{-5}$ Mpc^{-3} (1500/300) $\sim 1.5 \times 10^{-4}$ Mpc^{-3} $\sim n(> L^*$ ellipticals at $z \sim 0$). The measured average absolute magnitude of these high-z ULIRGs ($< M_K > \sim -26.4$ at $z \sim 2.2$) is consistent with that of $> L^*$ elliptical at $z \sim 0$, after taking into account the fading of the stellar population.

2.3.2 Black Hole Growth

The fraction of AGN (Seyfert nuclei) has long been known to increase with infrared luminosity, from about a third among ULIRGs with log[L$_{IR}$/L$_\odot$] $\sim$ 12 to about a half among ULIRGs with log[L$_{IR}$/L$_\odot$] $\geq$ 12.3 (e.g., Veilleux et al. 1995, 1999ab; Fig. 15). This trend is also seen at mid-infrared wavelengths (Lutz et al. 1999; Tran et al. 2001; Veilleux et al. 2008).

A detailed morphological study on local ULIRGs and PG QSOs conducted

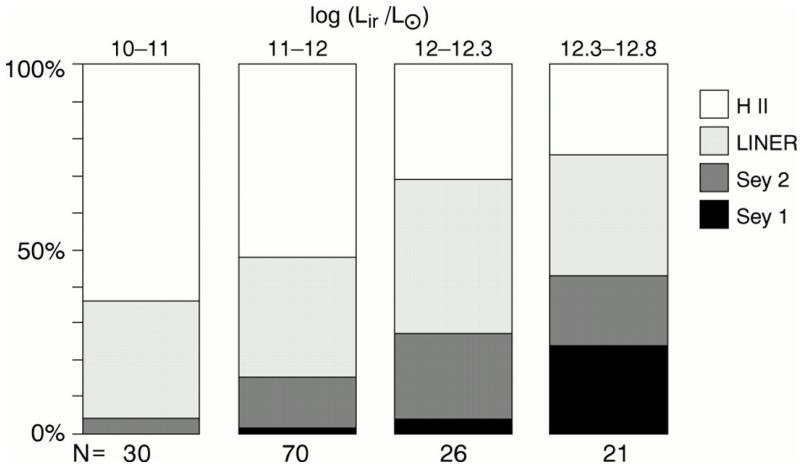

Fig. 15. The optical spectral classification of infrared galaxies versus infrared luminosity (From Veilleux et al. 1995, 1999a)

by our group (Veilleux et al. 2006) shows that (1) nearly all quasar-like ULIRGs are advanced mergers, (2) starburst-like ULIRGs are found in all merger phases, (3) warm, AGN-like ULIRGs live in early-type hosts, (4) tidal features are weaker among warm, AGN-like, early-type ULIRGs, and (5) the host sizes and luminosities of PG QSOs are statistically indistinguishable from those of the ULIRG hosts [in comparison, radio brighter quasars, such as those studied by Dunlop et al. (2003), have hosts which are larger and more luminous; Fig. 13]. All of these results, except #2, provide support for a possible merger-driven evolutionary connection between cool ULIRGs, warm ULIRGs, and PG QSOs. However, this sequence may break down at low luminosity since the lowest luminosity PG QSOs in the sample of Veilleux et al. (2006) show distinct disk components which preclude major (1:1 – 2:1) mergers. The presence of starburst-like ULIRGs in all merger phases seems to indicate that this merger scenario is not 100% efficient at producing an AGN.

A kinematic analysis of a dozen PG QSOs by our group (Dasyra et al. 2007) shows agreement between the host mass (thus black hole mass) of PG QSOs and coalesced ULIRGs (see Table 2). Converting the host dispersion in fully coalesced ULIRGs into black hole mass with the aid of the $M_{BH} - \sigma$ relation (e.g., Gebhardt et al. 2000) yields black hole mass estimates of the order $10^7 - 10^8$ $M_\odot$. The accretion rate for sources after the nuclear coalescence is high $0.5 - 0.9$, similar to those derived by Veilleux et al. (2002, 2006).

The situation at high redshifts is much less clear. Most (~ 50 – 75%) submm galaxies with $\log[L_{IR}/L_\odot] > 12.5$ harbor an AGN (Seyfert nucleus; Smail et al. 2002; Chapman et al. 2005), but apparently the AGN generally does not dominate the energy output in these systems (e.g. Alexander et al. 2005). This AGN fraction appears to increase with infrared luminosity, as in the case of their lower redshift counterparts (Sajina et al. 2007). The black hole mass

Table 2. Comparison of Local QSOs with Local ULIRGs

Class	$\log[L_{BOL}/L_\odot]$	m/m^*	$\log m_{BH}$	η_{Edd}
	...	($m^* = 1.4 \times 10^{11}$ $M_\odot$)	($M_\odot$)	
<ULIRG>	12.2	0.8	7.9	0.5
<PG QSOs>	12.2	1.5	8.0	0.3

in these systems is essentially unknown, except for X-ray estimates. At face value, the black hole to stellar mass ratios of high-z submm galaxies appears to be 1-2 orders of magnitude smaller than the local value, but this is only true if the black holes are accreting at the Eddington limit and are not Compton thick. This discrepancy is reduced by a factor of ~ 5 if the virial black-hole mass estimator is used, implying accretion at $\sim 20\%$ of the Eddington limit (Alexander et al. 2008).

2.4 Summary

The large body of data on local (distant) ULIRGs suggests that many of them are undergoing a major merger and are in the process of forming spheroids of intermediate (large) masses at $z \sim 0$ (2). The $> L^*$ ellipticals we see today may be the descendants of $z \sim 2$ ULIRGs. Black hole growth is clearly taking place along the merger sequence, and the results of detailed studies at low redshift provide support for an evolutionary connection between ULIRGs and *some* QSOs. However, it is not clear at present whether the end-result of high-z ULIRGs are indeed quasars. This evolutionary scenario requires that an important fraction of the gas mass be removed from the cores of these objects to reveal the QSOs. The presence of galactic winds may therefore be an important condition for this evolutionary scenario – this is the subject of Lecture #3 (§3).

3 Feedback Processes and their Impact on Galaxy Formation and Evolution

3.1 Introduction

Feedback processes likely have a strong impact on the formation of galaxies and their evolution of galaxies. These processes are divided into two broad categories: mechanical and radiative. In the first case, mechanical energy or momentum from starbursts and/or AGN affects the thermal and chemical

properties of galaxies over the entire galaxy mass spectrum. Radiative feedback may take several forms. Radiation pressure may be important near luminous starbursts and/or AGN. Radiative heating may also be dynamically important in luminous AGN, causing Compton-heated winds in the cores of these objects. Radiation may also ionize the surrounding ISM. Ionization cones in local AGN (Wilson & Tsvetanov 1994) and the proximity effect near QSOs (e.g., Bajtlik, Duncan, & Ostriker 1988) are direct consequences of this process. Radiation may also destroy molecules (H_2, polycyclic aromatic hydrocarbons [PAHs]) and cause dust grains to sublimate. This process is particularly important in dwarf galaxies at high redshifts.

The main focus of this lecture is mechanical feedback. Galactic winds are the primary mechanism by which energy and metals are recycled in galaxies and are deposited into the intergalactic medium. New observations are revealing the ubiquity of this process, particularly at high redshift. Here, I first describe the basic physics behind winds (§3.2), discuss the observational evidence for them in nearby star-forming and active galaxies (§§3.3 and 3.4) and in the high-redshift universe (§3.5), and consider the implications of energetic winds for the formation and evolution of galaxies (§3.6). Finally, in §3.7, I describe a series of unanswered questions which could possibly be tackled as PhD thesis projects. Much of the discussion is inspired from the review article by Veilleux, Cecil, & Bland-Hawthorn (2005) with recent updates when needed. For more detail on high-z winds, the readers should refer to Ferrara (2007).

3.2 Basic Physics of Mechanical Feedback

There are two possible sources of energy for mechanical feedback in galaxies: starbursts or AGNs. In starburst winds, the mechanical energy / momentum is provided either by stellar (OB, WR) winds or by supernovae. Their contributions are expected to scale with the star formation rate. In an instantaneous starburst, stellar winds are expected to dominate during the first $\sim 6 \times 10^6$ yrs and then SNe take over until ~ 40 Myr. AGN winds, on the other hand, may be driven by radiation pressure, radiative heating (Compton-heated wind; Begelman 1985), or magnetic fields anchored in the accretion disks. In this last case, the outflow is in the form of loosely (or highly) collimated jets depending on whether one is dealing with a radio-quiet (or radio-loud) AGN. The contributions to the winds are expected to scale roughly with the luminosity of the AGN or the mass accretion rate onto the supermassive black hole.

Thermalization of the mechanical energy by the starburst or the AGN creates a cavity of hot gas in the starburst or near the AGN with a temperature

$$T = 0.4\ \mu\ m_H\ \dot{E}/k\dot{M}, \tag{1}$$

where $\dot{E}$ is the fraction of the mechanical energy injection rate that is thermalized and $\dot{M}$ is the rate at which the mass is heated. For a starburst, equation (1) becomes:

$$T \approx 3 \times 10^8 \ \xi \ \Lambda^{-1} \ \ \mathrm{K}, \tag{2}$$

where ξ is the thermalization efficiency of the mechanical energy. The parameter Λ is the mass-loading factor, the ratio of the total mass of heated gas to the mass that is directly ejected by SNe and stellar winds or by the AGN. It accounts for the possibility that some of the ISM is mixed with the stellar or AGN ejecta. Note that this tenuous hot gas will be a poor X-ray (bremsstrahlung) emitter unless $\xi/\Lambda \ll 1$.

The pressure created by this hot gas can significantly exceed the pressure of the undisturbed ISM, hence drive the bubble outflow. Bubble evolution in gas-rich systems is described by the self-similar Taylor-Sedov solutions to a point-source explosion (blast wave) in a homogeneous medium (Taylor 1950; Sedov 1959). If radiative losses of the overall system are negligible, the expanding bubble is *energy-conserving* and the velocity of the expanding shell of shocked ISM are given by (Castor, McCray, & Weaver 1975; Weaver et al. 1977)

$$V_{\mathrm{shell}} = 640 \ (\xi \dot{E}_{44}/n_o)^{1/5} \ t_6^{-2/5} = 670 \ (\xi \dot{E}_{44}/n_o)^{1/3} \ r_{\mathrm{shell,kpc}}^{-2/3} \ \ \mathrm{km\ s^{-1}}, \tag{3}$$

where t_6 is the age of the bubble in Myr, n_o is the ambient density in $\mathrm{cm^{-3}}$, and $\dot{E}_{44}$ is the mechanical luminosity of the wind in units of 10^{44} erg $\mathrm{s^{-1}}$. Once the shell has formed, if the wind-blown bubble approaches the scale height of the disk H, the shell reaccelerates, begins to fragment through growing Rayleigh-Taylor instabilities, and finally vents these fragments and the freely flowing and shocked wind into the galaxy halo (e.g., Fig. 16). The terminal velocity of the wind can be estimated by equating the total energy deposition rate $\xi \dot{E}$ to the asymptotic rate of kinetic energy loss: $\frac{1}{2} \ \Lambda \dot{M} V_\infty^2 \approx \xi \dot{E}$. For a starburst-driven wind, we obtain

$$V_\infty \approx (2 \ \xi \dot{E}/\Lambda \dot{M})^{\frac{1}{2}} \approx 3000 \ (\xi/\Lambda)^{\frac{1}{2}} \ \ \mathrm{km\ s^{-1}}. \tag{4}$$

The Λ dependence is easy to understand: cold ISM gas that feels the full brunt of the wind is shock heated and evaporated and eventually mass loads the hot flow, which slows the wind. Equation (4) assumes negligible halo drag.

More relevant to the measured velocity of the line-emitting debris in the winds is the expected terminal velocity of clouds accelerated by the wind ram pressure

$$V(\mathrm{cloud}) \approx 600 \ \dot{p_{34}}^{0.5} \ \Omega_W^{-0.5} \ r_{0,\mathrm{kpc}}^{-0.5} N_{\mathrm{cloud},21}^{-0.5} \ \ \mathrm{km\ s^{-1}}, \tag{5}$$

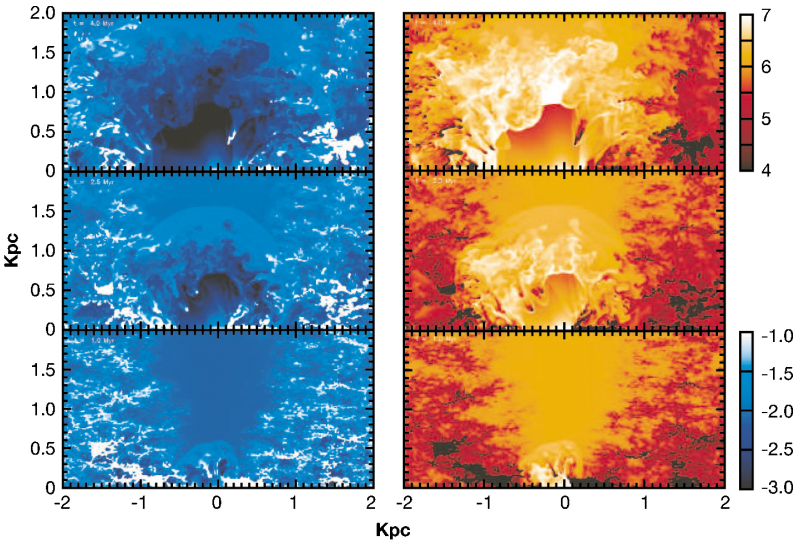

Veilleux, S et al. 2005
Annu. Rev. Astron. Astrophys. 43: 769–826

Fig. 16. An example of a state-of-the-art 3D hydrodynamical simulation of a starburst outflow in an interstellar media with fractal size distribution at three epochs after the constant energy input wind starts to blow: 1.0 Myr (bottom), 2.5 Myr (middle), and 4.0 Myr (top). Blue is log-density and red is log-temperature. (From Cooper et al. 2007)

where $\dot{p}_{34}$ is the wind momentum flux in units of 10^{34} dynes, $N_{\rm cloud,21}$ is the column density of the cloud in units of 10^{21} cm^{-2}, r_0 is the initial radius in kpc where the cloud is injected into the wind, Ω_W is the solid angle of the wind in steradians.

3.3 A Few Local Examples

3.3.1 The Milky Way Galaxy

Evidence is mounting for the existence of a nuclear wind in our own Milky Way Galaxy. Sofue & Handa (1984) discovered the 200-pc diameter Galactic Center radio lobe (GCL, Fig. 17), with an implied thermal energy of $\sim 3 \times 10^{51}$ erg. Bland-Hawthorn & Cohen (2003) detected the GCL at mid-IR wavelengths (Fig. 17). The association of the lobe with denser material raises the energetics to $10^{54}/\kappa$ erg, where κ is the covering fraction of the dense shell; less energy is needed if PAHs contribute significantly to the mid-iIR continuum emission. These energetics assume a shell velocity of ~ 150 km s^{-1}, a value based on the kinematics of the neighboring molecular gas after correction for bar streaming; this value is uncertain because of our location in the plane. The ROSAT 1.5 keV diffuse X-ray map over the inner 45° provides compelling evidence for this galactic wind interpretation (Fig. 17) (Bland-Hawthorn & Cohen 2003).

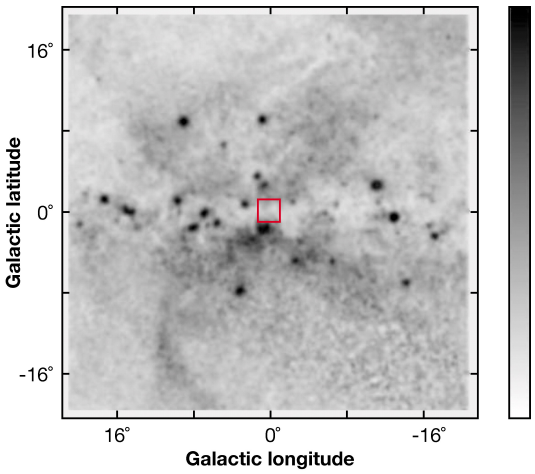

Veilleux, S et al. 2005
Annu. Rev. Astron. Astrophys. 43: 769–826

Fig. 17. Aspects of the Milky Way's wind. (Top) ROSAT 1.5 keV diffuse X-ray map that shows a biconical pattern emerging from the Galactic Center on scales of tens of degrees. (Bottom) The inner 2.52.5′ around the Galactic Center. Above, the plane in red is the Galactic Center Lobe, here imaged by Law & Yusef-Zadeh with rasters from the Green Bank Telescope. Elsewhere, the color image comes from 8.3 (B), 13 (G), and 21.3 (R) μm scans obtained with the SPIRIT III radiometer on the MSX spacecraft. These show embedded dust at various temperatures. Note the warm dust filaments along the edges of the GCL. (From Veilleux et al. 2005)

3.3.2 M82

M82 hosts arguably the best studied example of a galactic wind (Fig. 18). The bright Hα-emitting filaments above and below the disk of this object are moving at a deprojected velocity of 525 – 655 km s^{-1}. These filaments have a total mass of $\sim 5.8 \times 10^6$ M$_\odot$ and kinetic energy of $\sim 2.1 \times 10^{55}$ ergs, or about 1% of the total mechanical energy input from the starburst (Shopbell & Bland-Hawthorn 1998). Deep Hα and X-ray images of M82 reveal that the outflow

Veilleux, S et al. 2005
Annu. Rev. Astron. Astrophys. 43: 769–826

Fig. 18. M82, imaged by the Wisconsin Indiana Yale NOAO telescope in Hα (magenta) and HST in BVI continuum colors. Several of the largest scale filaments trace all the way back to super-starclusters embedded in the disk. (Courtesy Smith, Gallagher, & Westmoquette)

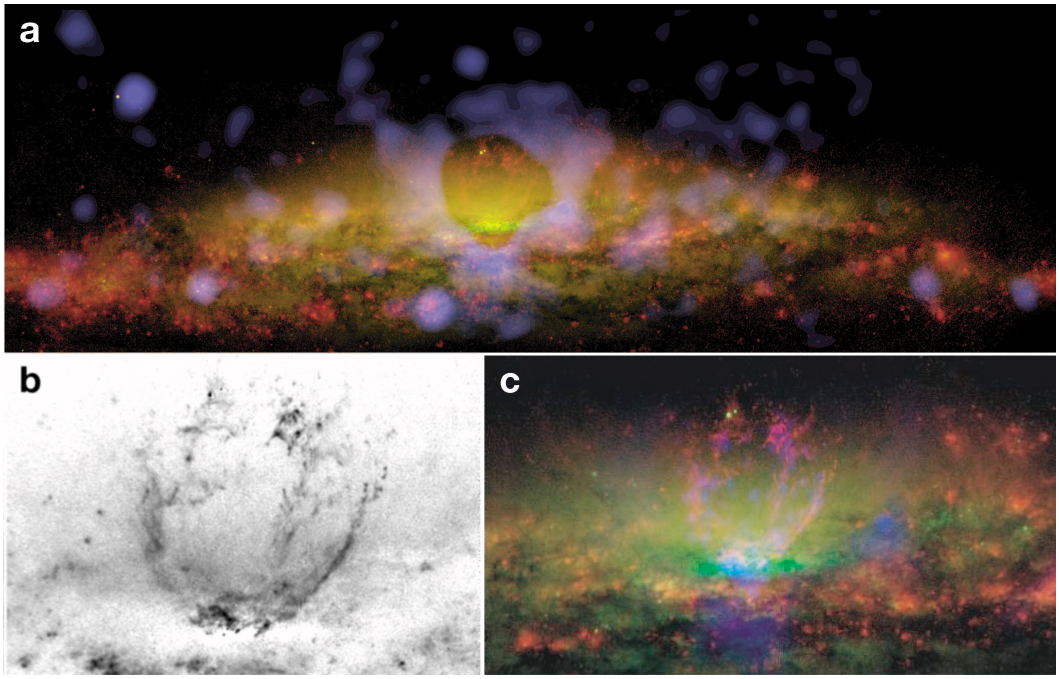

Veilleux, S et al. 2005
Annu. Rev. Astron. Astrophys. 43: 769–826

Fig. 19. NGC 3079 imaged with HST (red for Hα + [N II], green for I-band) and X-ray (blue). (a) Large-scale emission across 15 × 5 kpc. Numerous Hα filaments rise above the disk. Note the V-shaped wind pattern extending in X rays from the nucleus; for clarity, we have suppressed the diffuse X-ray emission across the superbubble, where it is generally clumped (c). (b) The 1 × 1.2 kpc superbubble in Hα + [N II] emission, with log-scaled intensities. It is composed of four vertical towers of twisted filaments; the towers have strikingly similar morphologies. (c) Close-up of the wind-swept, circumnuclear region. Note how X-ray emission (blue) clumps along the optical filaments of the superbubble at the limit of *Chandra*'s resolution. A prominent dust filament at left drops out of the wind. (From Veilleux et al. 2005)

extends at least 12 kpc from the nucleus, some of which may be escaping from the galaxy (e.g., Devine & Bally 1999; Lehnert et al. 1999; Stevens, Read, & Bravo-Guerrero 2003). Walter, Weiss, & Soville (2002) also found that $\sim 3 \times 10^8$ $M_\odot$ of molecular gas is taking part in this outflow, corresponding to a kinetic energy $\sim 3 \times 10^{55}$ ergs, very similar to that of the bright Hα filaments.

3.3.3 NGC 3079

The best known example of a "young" outflow is found in NGC 3079, where a partially ruptured 1-kpc superbubble is powered by a nuclear starburst (Fig. 19). The outflow velocity of the warm ionized gas is a record-setting $\sim$ 1500 km s^{-1}. The superbubble is composed of 4 vertical towers of twisted filaments;

the towers have strikingly similar morphologies and are made of gas in vortex motion like that of a mushroom cloud from an atomic bomb explosion (Veilleux et al. 1994; Cecil et al. 2001; Cecil, Bland-Hawthorn, & Veilleux 2002).

3.3.4 Hot Wind Fluid

Chemically-enriched wind fluid has been directly observed in X-rays in very few objects: the Milky Way (Yuasa et al. 2007), M82 (Griffiths et al. 2000; Stevens et al. 2003), and possibly NGC 1569 (Martin, Kobulnicky, & Heckman 2002). The fairly modest alpha-element to iron ratio seems to imply substantial mixing of the supernova-processed material with the ambient ISM.

3.3.5 Dust Outflow

There is now direct evidence that dust also participates in galactic-scale outflows. The best example so far is that of M82 seen by GALEX (Hoopes et al. 2005) and Spitzer (Engelbracht et al. 2006; Fig. 20). Galactic winds therefore provide another way (other than galaxy interactions, for instance) to bring dust out of galaxies and into the intergalactic medium.

3.4 Statistics on Winds at $z < 0.5$

Here we summarize the properties of local galactic winds. See Veilleux et al. (2005) for more detail.

- Starburst-driven winds require a star formation rate above $\sim$ few $M_\odot$ yr^{-1} or a star formation rate surface density (averaged over the optical size of the galaxy) larger than ~ 0.001 $M_\odot$ yr^{-1} kpc^{-2}.
- AGN-driven winds are seen in most radio-loud AGN and $\geq 1/3$ of all radio-quiet AGN.
- They subtend a solid angle $\Omega_{\rm wind}/4\pi \sim 0.1 - 0.5$
- They extend to a radius of a few to more than 50 kpc.
- The deprojected outflow velocities range from ~ 25 km s^{-2} in dwarf galaxies to more than 1000 km s^{-1} in the more powerful starbursts. This velocity depends on the star formation rate (Fig. 21) and the gas phase under consideration (it increases with the temperature of the gas).
- The mass outflow rates in starbursts $dM/dt_{\rm outflow} = \beta$ SFR where the entrainment efficiency $\beta \sim 0.01 - 5$ and "saturates" at the highest SFR.
- The mass outflow rates in AGNs exceeds the mass accretion rates onto the SMBH.
- The escape fraction of the gas is poorly constrained. It depends on the temperature of the gas and the importance of the halo drag. Neglecting

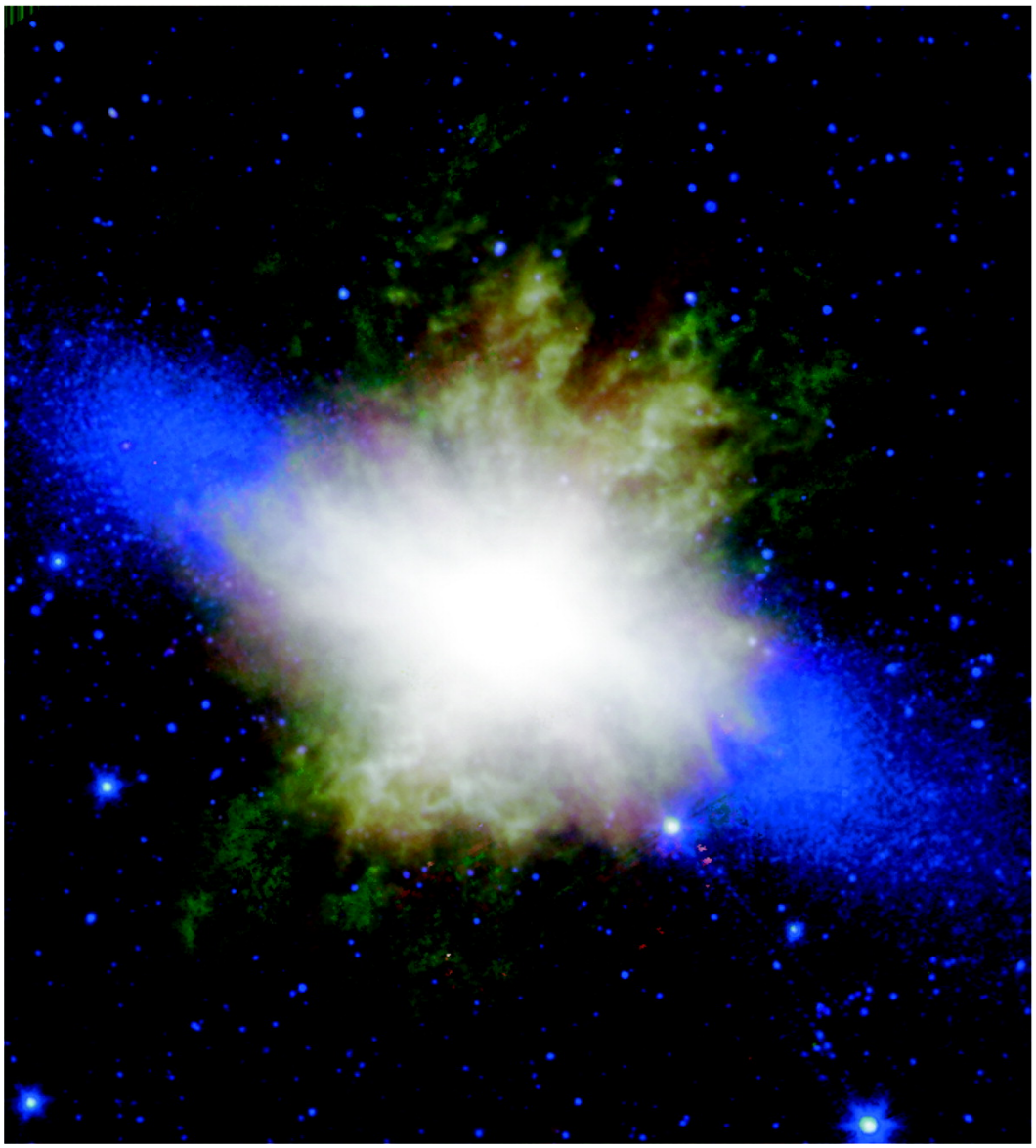

Fig. 20. Color-composite image of M82, displayed with a logarithmic stretch. The blue channel is the IRAC 3.6 μm image and the green channel is the IRAC 8.0 μm image (= PAH/dust emission), while the red channel is the MIPS 24 μm image, where the bright nucleus and associated diffraction spikes have been subtracted; the radial red streaks are residuals of the subtraction. The panel is $9.2' \times 9.2'$ on a size, or 9.6×10.7 kpc. (From Engelbracht et al. 2006)

halo drag, current numbers for the outflowing neutral gas are ~ 5 – 20%. It is likely higher for the hotter gas phase.

- The kinetic energy involved in starburst-driven outflows is 10^{53} – 10^{59} ergs $\sim (10 - 50\%)$ of the total kinetic energy returned to th ISM by the starburst. It scales roughly with the star formation rate.
- The kinetic energy involved in AGN-driven outflows is similar to that starburst-driven outflows. It scales with the power of the AGN. A rough rule of thumb

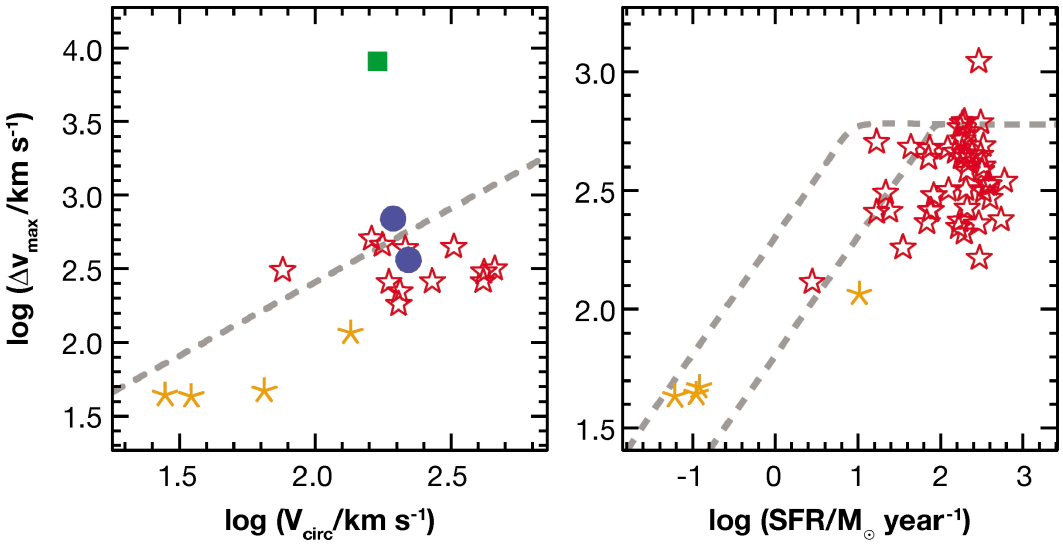

Veilleux, S et al. 2005
Annu. Rev. Astron. Astrophys. 43: 769–826

Fig. 21. Maximum Na I D absorption-line outflow velocities as a function of (a) circular velocities and (b) star formation rates. Orange skeletal stars represent star–forming dwarfs from Schwartz & Martin (2004), and red open stars represent infrared-selected starbursts from Rupke, Veilleux & Sanders (2005a,b). Filled blue circles and filled green square represent Seyfert 2s and Seyfert 1s, respectively, from Rupke, Veilleux & Sanders (2005c). The dashed line in panel a represents the escape velocity for a singular isothermal sphere with $r_{\rm max}/r = 10$, whereas the dashed lines in panel b are characteristic velocities of ram-pressure accelerated clouds (Murray et al. 2005) for column densities of 10^{20} cm^{-2} (top line) and 10^{21} cm^{-2}. (From Veilleux et al. 2005)

for the jet mechanical luminosity is $\sim 0.1\ L_{\rm Eddington}$.

- The energy stored in radio lobes of powerful radio galaxies reaches $\sim 10^{58}$ – 10^{61} ergs.

3.5 High-z Winds

There is evidence for winds in the spectra of several $z > 1$ galaxies. Low-ionization interstellar absorption lines that are blueshifted by hundreds of km s^{-1} relative to systemic velocities, and Lyα emission lines similarly shifted redward, have been detected in most $z \sim 3-4$ Lyman break galaxies (LBGs), in several gravitationally lensed Lyα-emitting galaxies at $z \sim 4-5$, and in many luminous infrared galaxies at $z \geq 2$. Lyα emission with red asymmetric or P Cygni-type profiles is also commonly seen in $z \geq 5$ Lyα-emitting galaxies. Outflow velocities of ~ 300 km s^{-1} are typically observed in LBGs (e.g., Shapley et al. 2003). This value is slightly higher than the outflow velocities found in low-z galaxies of similar star formation rates. Spectral analyses of

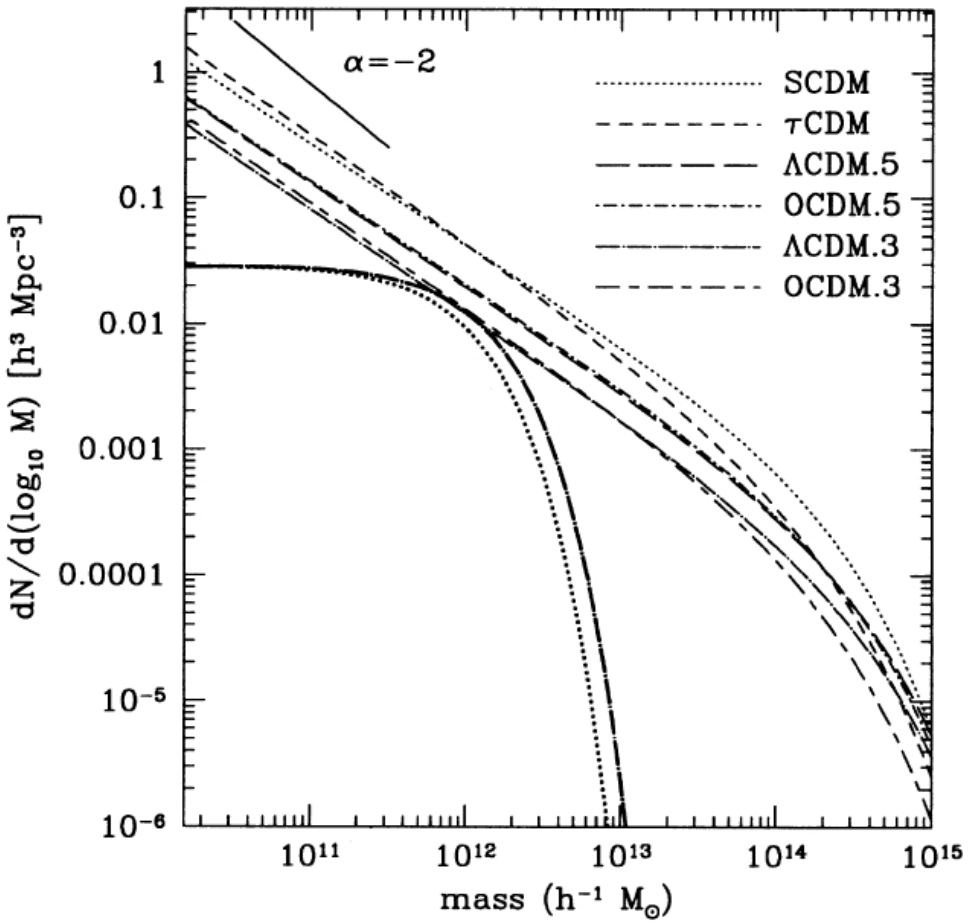

Fig. 22. The mass function of dark matter haloes predicted for various CDM cosmologies (light broken lines). The bold lines show the mass function of galactic haloes. Note the large discrepancy in slopes at small and large masses. (from Somerville & Primack 1999)

background QSOs with line-of-sights near the LBGs provide new constraints on the environmental impact of LBG winds. Adelberger et al. (2005) found significant HI deficits within 1 Mpc of $\sim 1/3$ of LBGs. These results are qualitatively consistent with the idea that winds emerge along paths of least resistance out of 500 kpc, avoiding large-scale filaments.

3.6 Impact on Galaxy Formation and Evolution

There is growing evidence that galactic winds have inhibited early star formation and have ejected a significant fraction of the baryons once found in galaxies. The latter may explain why few baryons are in stars ($\Omega_*/\Omega_b \sim 0.1$; Fukugita, Hogan, & Peebles 1998) and why galaxies like the Milky Way contain fewer baryons than expected from hydrodynamical simulations (Silk 2003). We

review in this section the impact of winds on galaxies and on their environment.

3.6.1 Galaxy Luminosity Function

Galactic winds have modified substantially the shape of the galaxy luminosity function, flattening its faint-end slope compared to that of the halo mass function (Fig. 22). Significant feedback also appears necessary to avoid the 'cooling catastrophe' at high redshift that would otherwise overproduce massive luminous galaxies (Fig. 22). Energies of a few $\times\ 10^{49}$ ergs per solar mass of stars formed can explain the sharp cutoff at the bright end of the luminosity function. Starburst-driven winds are too feeble by a factor of several to fully account for the cutoff. It is therefore argued that feedback from black hole accretion is the only way to expel winds hot enough to prevent subsequent gas recapture by group halos. Feedback from starburst- and AGN-driven winds may help set up the bi-modality observed in galaxy properties (blue & red sequences). AGN feedback may be particularly effective in clustered environment where the infalling gas is heated by a virial shock and thus more dilute.

3.6.2 Black Hole – Spheroid Connection

As discussed in Lecture # 1 (§1), a mechanism is needed to regulate the growth of the black hole and the starburst and produce the black hole – spheroid mass relation. Negative feedback from AGN- and/or starburst-driven winds may be responsible for stopping the gas flow to the AGN and the surrounding starburst (e.g., Murray et al. 2005).

3.6.3 Mass – Metallicity Relation

Galactic winds may help explain the well-known galaxy mass – metallicity relation. In this scenario, massive galaxies with deep gravitational potentials are expected to retain more of their supernova ejecta than dwarf galaxies. An analysis of the Sloan Digital Sky Survey (SDSS) database by Tremonti et al. (2004) has shown that the gas-phase metallicity of local star-forming galaxies increases steeply with stellar mass from $10^{8.5}$ to $10^{10.5}$ $\mathrm{M}_{\odot}h_{70}^{-2}$, but flattens above $10^{10.5}$ $\mathrm{M}_{\odot}h_{70}^{-2}$. Similar trends are seen when internal velocity or surface brightness is considered instead of stellar mass (Kauffmann et al. 2003a). The stellar mass scale of this flattening coincides roughly with the dynamical mass scale of metal retention derived by Garnett (2002). These results suggest that the chemical evolution of galaxies with $v_c \geq 125$ km s^{-1} is (virtually) unaffected by galactic winds, whereas galaxies below this threshold tend to lose a large fraction of their supernova ejecta.

3.6.4 Influence on Intergalactic Scales

Galaxy winds from early galaxies have been proposed to explain the "entropy floor" of galaxy clusters, the metal abundances of the intracluster and intergalactic media, and the lack of massive cooling flows in rich galaxy clusters with (once) powerful radio galaxies.

3.7 Open Issues

The questions in this section are directly taken from Veilleux et al. (2005) but they are updated to take into account papers published in the past three years. Each of these questions could be a worthwhile PhD thesis project.

3.7.1 Theoretical Challenges

1. Modeling the energy source. Current simulations do a poor job of modeling the energy source itself, especially in AGN-driven winds where energy and momentum injection rates and their dependence on mass accretion rate are virtually unknown.
2. Modeling the host ISM. The recent work of Cooper et al. (2007) is the first of a new generation of simulations able to handle a multiphase ISM with a broad range of densities and temperatures. Such sophistication is crucial to understanding and predicting the mass of gas entrained in winds.
3. Coupling the radiation field to the gas. Current simulations do not account for possible coupling between the wind material and the radiation field emitted by the energy source or the wind itself, and indeed ignore radiation pressure.

3.7.2 Observational Challenges

1. Hot wind fluid. This component drives starburst-driven winds, yet has been detected in very few objects. Metal abundances suggest enrichment by Type II supernovae, but the measurements are highly uncertain. Both sensitivity and high spatial resolution are needed to isolate the hot wind fluid from X-ray stellar binaries and the rest of the X-ray-emitting gas. But, no such instrument is planned for the foreseeable future.
2. Entrained molecular gas and dust. Despite the important role of the molecular component in galactic winds, high-quality mm-wave data exist only for M82. This is due to the limited sensitivity and spatial resolution of current instruments, but this is changing. New mm-wave arrays (e.g., CARMA, and especially ALMA) will map the molecular gas in a large sample of nearby

galaxies with excellent resolution ($< 1''$). As described in §3.3.5, Spitzer has recently helped constrain the amount and location of dust in the winds.

3. Zone of influence and escape efficiency. Current estimates of these two quantities are limited by the sensitivity of the instrument used for the measurements. Deeper emission-line, X-ray, and radio maps of wind galaxies will provide better constraints on the extent of the wind and the probability that the outflowing material escapes from the potential well of the host.
4. Thermalization efficiency. Observational constraints on the thermalization efficiency of GWs are rare because of an incomplete accounting of the various sources of thermal energy and kinetic energy in the wind. A multiwavelength approach that considers all gas phases is needed.
5. Wind / ISM interface and influence of magnetic fields. Constraints on microphysics at the interface between the wind and galaxy ISM are available in only a handful of galaxies. High-resolution ($\leq$ parsec scale) imaging and spectra of the entrained disk material in a sizable sample of local objects are required. The large-scale morphology of the magnetic field lines has been mapped in a few winds, but the strength of the field on pc scale is unknown. This information is crucial in estimating the conductivity between the hot and cold fluids.
6. Positive feedback. Star-forming radio jet/gas interactions have been found in a few nearby systems and are suspected to be responsible for the "alignment effect" between the radio and UV continua in distant radio galaxies. The same physics may also provide positive feedback in wind galaxies. Convincing evidence for positive feedback has been found in the disk of M82 (Matsushida et al. 2004), but the frequency of this phenomenon is completely unknown.
7. Galactic winds in the distant universe. Absorption-line studies of high-z galaxies and QSOs will remain a powerful tool to search for distant galactic winds and to constrain their environmental impact. Future large ground and space telescopes will extend such studies to the reionization epoch. These galaxies are very faint, but gravitational lensing by foreground clusters can make them detectable and even spatially resolved.

4 Elemental Abundances as Tracers of Star Formation

4.1 Introduction: Basics of Chemical Evolution

Hydrogen, helium, and traces of lithium, boron, and beryllium were produced early on in the Big Bang. All other elements (*i.e.* all other "metals") were produced through nucleosynthesis in stars. The abundances of these elements are therefore a direct tracer of past star formation in a galaxy.

Gas is transformed into stars. Each star burns hydrogen and helium in its nucleus and produces heavy elements. These elements are partially returned into the interstellar gas at the end of the star's life via stellar winds or supernovae explosions. Some fraction of the metals are locked into the remnant of the star. If there is no gas infall from the outside or selective loss of metals to the outside, the metal abundance of the gas, and of subsequent generations of stars, should increase with time. So in principle the evolution of chemical element abundances in a galaxy provides a clock for galactic aging. One should expect a relation between metal abundances and stellar ages. On average, younger stars should contain more iron than older stars. This is partially the case for the solar neigborhood, where an age-metallicity relation is seen for nearby disk stars, but a lot of scatter is seen at old ages ($>$ 3 Gyr; e.g., Nordstrom, Andersen, & Mayor 2005). Clearly, our Galaxy is not as simple as described here and we need to add a few more ingredients to better match the observations.

In §4.2, I describe a few simple models to account for the complexity of galaxies. An extensive literature exists on this topic. I refer the readers to the seminal paper by Tinsley (1980) as well as Binney & Tremaine (1987; §§9.2 and 9.3) and Binney & Merrifield (1998; §5.3). In §4.3, I compare the predictions of these models with the observations in local star-forming and starburst galaxies and in distant star-forming galaxies and quasars. These comparisons help us understand the integrated star formation history and chemical evolution of these objects.

4.2 Simple Models

All models discussed here assume that the galaxy's gas is well-mixed *i.e.* uniform metal abundance, and that the (high-mass) stars return their nucleosynthetic products rapidly, much faster than the time to form a significant fraction of the stars (this is called the "instantaneous recycling approximation").

4.2.1 Closed Box

The closed-box model further assumes that no infall or outflow is taking place. In that case, the total baryonic mass of the galaxy, $M_{baryons} = M_{g(as)} + M_{s(tar)}$ = constant. If Z is the fraction by mass of heavy elements (the Sun's abundance is $Z_\odot \sim 0.02$ and the most metal-poor stars in the Milky Way have $Z \leq 10^{-4}\ Z_\odot$), the mass of heavy elements in the gas $M_h = ZM_g$.

If the total mass made into stars is dM_s' and the amount of mass instantaneously returned to the ISM (from supernovae and stellar winds, enriched with metals) is dM_s'', then the net matter turned into stars is $dM_s = dM_s' - dM_s''$.

The mass of heavy elements returned to the ISM is $y\ dM_s$, where y is the yield of heavy elements (made instantaneously). As a rule-of-thumb, only stars more massive than ~ 8 $M_\odot$ make heavies (supernovae). The fraction of mass returned to the ISM $dM_s''/dM_s \sim 0.20$, the yield $y \sim 0.01$ (dependent on stellar evolution and the Initial Mass Function $\equiv$ IMF), and the metallicity of the shed gas Z(shed gas) = (heavies shed) / (mass shed) = $y\ dM_s/dM_s'' \sim 0.01/0.2 = 0.05$ (*i.e.* about $2.5 \times Z_\odot$).

In the closed-box model, mass conservation implies

$$dM_g + dM_s = 0 \tag{6}$$

The net change in metal content of the gas is

$$dM_h = y dM_s - Z dM_s = (y - Z) dM_s \tag{7}$$

Since $dM_g = -dM_s$ and $Z = M_h/M_g$, the change in Z is

$$\begin{aligned} dZ &= dM_h/M_g - M_h dM_g/M_g^2 \\ &= (y - Z) dM_s/M_g + (M_h/M_g)(dM_s/M_g) = y dM_s/M_g \\ dZ/dt &= -y(dM_g/dt)/M_g \end{aligned}$$

Assuming y = constant (*i.e.* independent of time and Z):

$$\begin{aligned} Z(t) &= Z(0) - y \ln [M_g(t)/M_g(0)] \\ &= Z(0) - y \ln \mu(t), \end{aligned} \tag{8}$$

where μ = gas (mass) fraction $\equiv M_g(t)/M_g(0) = M_g(t)/M_t$. The metallicity of the gas grows with time, as new stars are formed and the gas is consumed.

The mass of the stars that have a metallicity less than $Z(t)$ is

$$M_s[< Z(t)] = M_s(t) = M_g(0) - M_g(t) = M_g(0)\ [1 - e^{-(Z(t)-Z(0))/y}] \tag{9}$$

When all of the gas has been consumed, the mass of stars with metallicity between $Z, Z + dZ$ is $dM_s(Z) \propto e^{-(Z-Z(0))/y} dZ$. This exponential drop-off reproduces well the metallicity distribution of stars in the bulge of our Galaxy (e.g., Rich 1990).

The yield y can be derived from observations:

$$Z(\text{today}) \sim Z(0) - y \ln[M(_g(\text{today})/M_g(0)] \tag{10}$$

The average metal content of the gas in the disk near the Sun is $Z \sim 0.7 Z_\odot$. The initial mass of gas $M_g(0) = M_s(\text{today}) + M_g(\text{today})$ where $M_s(\text{today}) \sim 40\ M_\odot\ \text{pc}^{-2}$ and $M_g(\text{today}) \sim 10\ M_\odot\ \text{pc}^{-2}$. Assuming that $Z(0) = 0$, we derive $y \sim 0.43\ Z_\odot$. Given this value for the yield, we can compute the mass in stars with $Z < 0.25 Z_\odot$ compared to the mass in stars with the current metallicity of the gas:

$$M_s(< 0.25 Z_\odot)/M_s(< 0.7 Z_\odot) = [1 - e^{-0.25 Z_\odot/y}]/[1 - e^{-0.7 Z_\odot/y}] \sim 0.54 \quad (11)$$

Therefore, half of all stars in the disk near the Sun should have $Z < 0.25\ Z_\odot$. However, only 2% of the F-G (old) dwarf stars in the solar neighborhood have such metallicity. This discrepancy is known as the "*G-dwarf problem*". Possible solutions to this problem include (1) pre-enrichment in the gas: $Z(0) \sim 0.15 Z_\odot$, (2) outflow (leaky-box model), and (3) infall (accreting-box model). Solutions (2) and (3) are described next.

4.2.2 Leaky Box

If there is an outflow of processed material, $g(t)$, the conservation of mass (Eq. 6) becomes:

$$dM_g/dt + dM_s/dt + g(t) = 0 \quad (12)$$

And the rate of change in the metal content of the gas mass (Eq. 7) now becomes:

$$dM_h/dt = y dM_s/dt - Z dM_s/dt - Z g(t) \quad (13)$$

As a first-order approximation, one can assume that the rate at which the gas flows out of the box is proportional to the star formation rate: $g(t) = c\, dM_s/dt$, where c is a constant. In Lecture #3 (§3.4), I noted that $c = 0.01 \rightarrow 5$ in starburst galaxies. In that case, one finds that $dZ/dt = [y/M_g(t)] dM_s/dt$, where $dM_s/dt = -(1/(1+c))(dM_g/dt)$, so $dZ/dt = -[y/(1+c)](1/M_g)(dM_g/dt)$. Integrating this equation, we get

$$Z(t) = Z(0) - [y/(1+c)] * \ln[M_g(t)/M_g(0)] \quad (14)$$

Comparing with Eq. (8), the only effect of an outflow is therefore to reduce the yield to an *effective yield* $= [y/(1+c)]$.

4.2.3 Accreting Box

Here we only consider the case of accretion of pristine (metal-free) gas to the box. Since the gas is pristine, Eq. (7) is still valid: the mass of heavy elements produced in a star formation episode is

$$dM_h/dt = (y - Z)dM_s/dt \tag{15}$$

However, Eq. (6) for the conservation of mass in the box becomes:

$$dM_g/dt = -dM_s/dt + f(t), \tag{16}$$

where $f(t)$ is the accretion rate. Consider the simple case in which the mass in gas in the box is constant. This implies then

$$\begin{aligned} dZ/dt &= (1/M_g)[(y - Z)dM_s/dt - ZdM_g/dt] \\ &= (1/M_g)[(y - Z)dM_s/dt] \end{aligned} \tag{17}$$

Integrating this equation and assuming that $Z(0) = 0$,

$$Z = y[1 - e^{-M_s/M_g}] \tag{18}$$

Therefore when $M_s >> M_g$, the metallicity $Z \sim y$. The mass in stars that are more metal-poor than Z is

$$M_s(< Z) = -M_g \ln (1 - Z/y) \tag{19}$$

In this case, for $M_g \sim 10\ M_\odot\ \mathrm{pc}^{-2}$ and $M_s \sim 40\ M_\odot\ \mathrm{pc}^{-2}$, and for $Z = 0.7\ Z_\odot$, then $y \sim 0.71\ Z_\odot$. Thus the fraction of stars more metal-poor than $0.25\ Z_\odot$ is $M(< 0.25)/M(< 0.7) \sim 10\%$, in much better agreement with the observations of the solar neighborhood.

4.3 Applications

It is technically easier to determine the chemical abundances in the ISM than in stars so I only discuss the results on the gaseous component of galaxies here. Elemental abundances in the ISM are subject to major uncertainties so it is instructive to describe briefly the general principles behind these measurements (interested readers should refer to Edmunds & Pagel 1984; McGaugh 1991; Kewley & Dopita 2002; Rupke, Veilleux, & Baker 2008 for more detail). All measurements rely on the relative strength of the various emission lines

produced by the gas heated and ionized by nearby hot, young stars. The basic idea is to determine the abundance of each ionic species and add them up to get the total abundance of a particular element, e.g., for oxygen: O/H = O^0/H + O^+/H + O^{++}/H + ... where H stands for the sum of neutral and ionized hydrogen. Unfortunately, only a certain number of lines are strong enough to be detected, so one often has to apply an ionization correction for the species that are not directly observed. These strong-line diagnostics are calibrated against photoionization models, electron temperature measurements (*i.e.* weak-line diagnostics), or a combination of the two. Different line diagnostics, or different calibrations of the same diagnostic, can give vastly different abundances for the same galaxy or group of galaxies. So it is important when comparing different galaxies to rely on the same line diagnostic with the same calibration. The most commonly used strong-line diagnostics are $R_{23} \equiv \{f([\mathrm{O\ II}]\ \lambda\lambda 3726, 3729) + f([\mathrm{O\ III}]\ \lambda\lambda 4959, 5007)\}/f(\mathrm{H}\beta)$ (Fig. 23) and $O_{32} \equiv f([\mathrm{O\ III}]\ \lambda\lambda 4959, 5007)/f([\mathrm{O\ II}]\ \lambda\lambda 3726, 3729)$. The latter is a proxy for the ionization parameter, which is the ratio of ionizing photons to hydrogen nuclei present in the gas. The $f([\mathrm{N\ II}]\ \lambda 6583)/f([\mathrm{O\ II}]\ \lambda\lambda 3726, 3729)$ and $f([\mathrm{N\ II}]\ \lambda 6583)/f([\mathrm{S\ II}]\ \lambda\lambda 6716, 6731)$ ratios have also been used with some success as metallicity indicators.

With these words of caution, I now proceed to describe the results of recent analyses on local and distant galaxies.

4.3.1 Local Star-Forming Galaxies

There is a well-known mass – metallicity relation among local star-forming galaxies. Figure 24 shows the results from an analysis of 53,000 SDSS galaxies (Tremonti et al. 2004). As described in Lecture #3 (§3.6.3) , this mass-metallicity relation is naturally explained by a leaky-box model which involves selective loss of metals via a galactic-scale outflow. Winds are more efficient at removing metals from shallower galaxy potential wells ($V_{rot} < 150$ km s^{-1}; Garnett 2002) and the effective yield $y_{\rm eff} = [1/(1+c)]y$ is smaller for smaller galaxies.

The well-known metallicity – radius relation *within* galaxies also favors leaky-box models on a *local* scale. Figure 25 shows the recent results from Kennicutt, Bresolin, & Garnett (2003) on M 101 (see also Zaritsky, Kennicutt, & Huchra 1994).

4.3.2 Local Powerful Starburst Galaxies

In a recent study of local luminous and ultraluminous infrared galaxies (LIRGs and ULIRGs, respectively; see definitions in Lecture # 2; §2.1), Rupke et al. (2008) have found that the oxygen abundances (and effective yields) in the

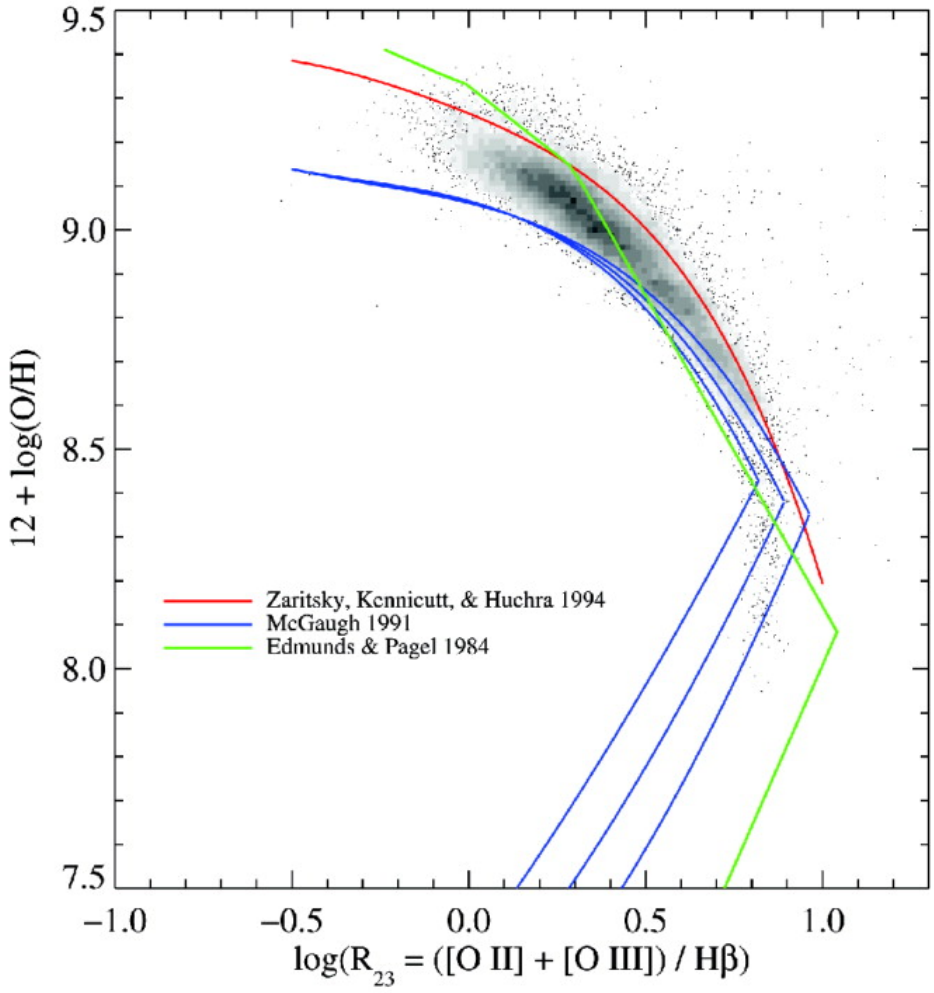

Fig. 23. Comparison of the relation between metallicity and the line ratio [O III] / [O II]. The blue line shows the theoretical calibration of McGaugh (1991) for three representative values of [O III]/[O II]. The green line shows the empirical calibration of Edmunds & Pagel (1984), and the red line shows the semiempirical calibration of Zaritsky et al. (1994), itself the average of three previous calibrations. (From Tremonti et al. 2004)

cores of these objects lie significantly below the [O/H] – host luminosity relation of local star-forming galaxies (Fig. 26). They find that this effect increases with increasing infrared luminosity (which is a proxy for the star formation rate in the starburst; Fig. 27). They conclude that the observed underabundance and smaller yield result from the combination of a decrease of abundance with increasing radius in the progenitor galaxies and strong, interaction- or merger-induced gas inflow into the galaxy nucleus. This conclusion demonstrates that local abundance scaling relations are not universal, a fact that must be accounted for when interpreting abundances earlier in the universe's history, when merger-induced star formation was the dominant mode (next

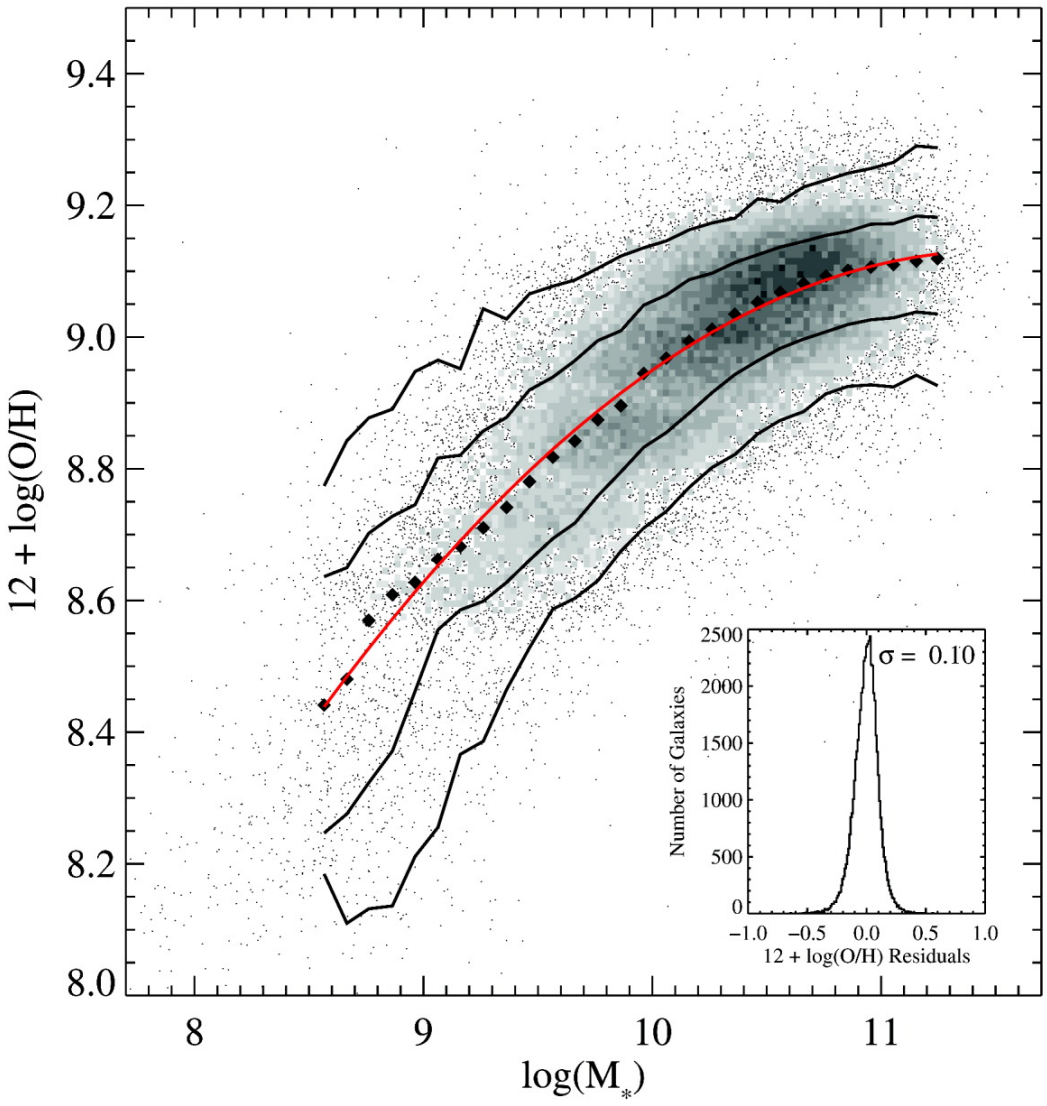

Fig. 24. Relation between stellar mass, in units of solar masses, and gas-phase oxygen abundance for 53,400 star-forming galaxies in the SDSS. The large black filled diamonds represent the median in bins of 0.1 dex in mass that include at least 100 data points. The solid lines are the contours that enclose 68% and 95% of the data. The red line shows a polynomial fit to the data. The inset plot shows the residuals of the fit. (From Tremonti et al. 2004)

section).

4.3.3 Distant Galaxies

The mass-metallicity relation of distant galaxies appears to fall below that of local galaxies. This is seen at $0.3 < z < 1$ (e.g., Kobulnicky & Kewley 2004; Savaglio et al. 2005) and at higher redshifts (e.g., Erb et al. 2006; Fig. 28). This result is usually interpreted as being due to a redshift evolution – in a

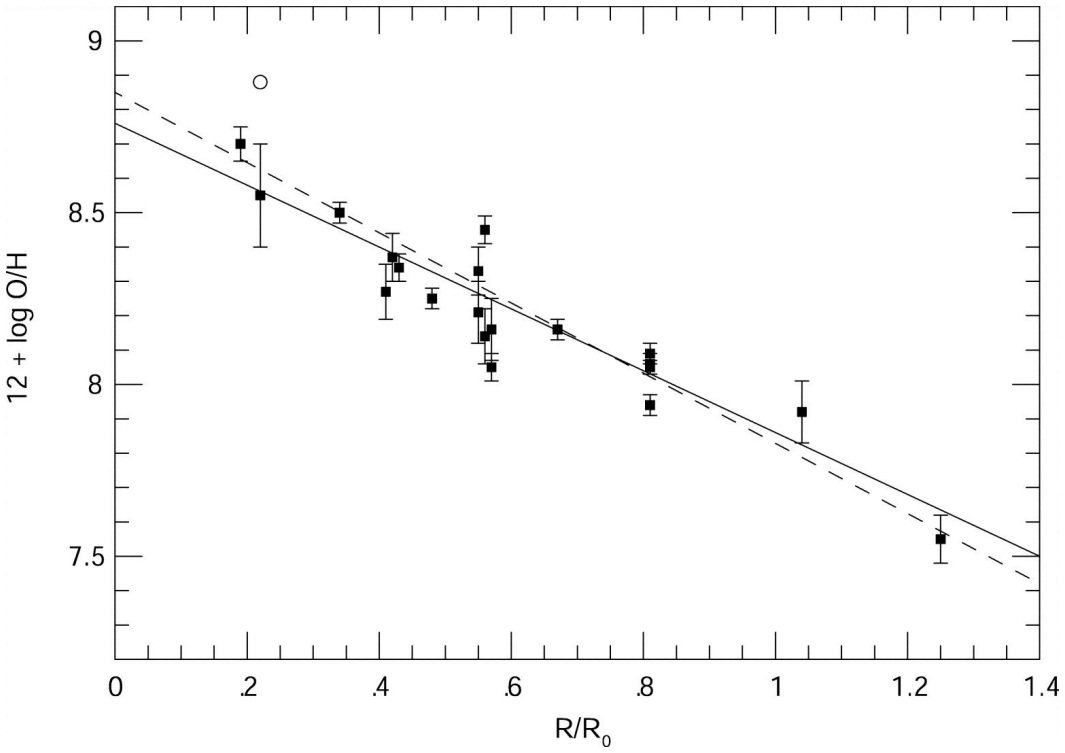

Fig. 25. Oxygen abundance gradient in M101 from 20 H II regions with electron temperature measurements. The linear fit to the data is shown by the solid line. (From Kennicutt et al. 2003)

closed box model, the metallicity builds up with time. However, the results discussed in §4.3.2 raise a red flag when interpreting the data at high redshifts. It may be once again that lower abundances (and effective yield) are due at least in part to merger-induced gas inflows. Rupke et al. (2008) have tried to address this issue by comparing galaxies with the same infrared luminosity at different redshifts. They found that the oxygen abundance of LIRGs increases by ~ 0.2 dex from $z \sim 0.6$ to $z \sim 0.1$ (Fig. 29), while modest if any evolution was found between $z \sim 2$ submm galaxies, $z \sim 0.5$ ULIRGs and the local $z \sim$ ULIRGs.

4.3.4 Distant Quasars

Emission lines in distant quasars have been used successfully to estimate the nuclear gas metallicity of the galaxy hosts. The most luminous QSOs have nuclear metallicities typical of giant ellipticals. A trend of increasing metallicity with increasing luminosity has been found (e.g., Hamann & Ferland 1999; Fig. 30). This may be equivalent to the mass-metallicity measured at low redshift. However, interestingly, Shemmer et al. (2004) have found that metallicity is even more strongly correlated with accretion rate onto the black hole (which is a function of luminosity *and* Hβ line width; Fig. 31). This may imply an intimate relation between starbursts, responsible for the enrichment of the

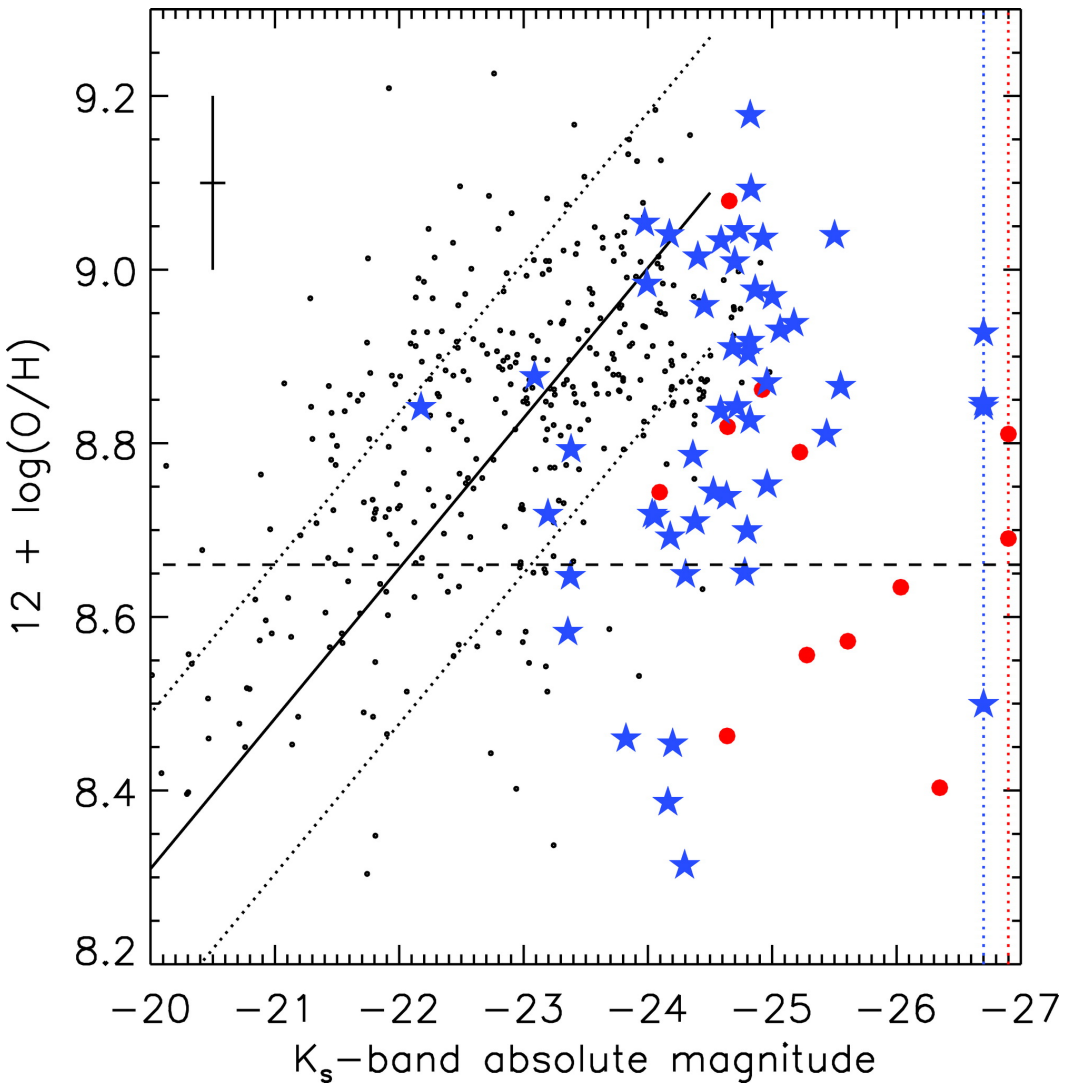

Fig. 26. Ks-band luminosity-metallicity relation for nearby emission-line galaxies (small black circles), LIRGs (blue stars), and ULIRGs (red circles). Most of the LIRGs and ULIRGs fall well below the L-Z relation. The nearby galaxies are from the KISS sample, and the black line and dotted lines are a fit to the data and 1 σ rms dispersion, respectively (Salzer et al. 2005). The dashed line locates solar abundance. The far-right points do not have measured K-magnitudes. The error bars represent the scatter in the abundance-R23 relation that was used to compute LIRG and ULIRG abundances, as well as the standard deviation in the ULIRG mass distribution. (From Rupke et al. 2008)

nuclear gas, and AGN fueling, represented by the accretion rate.

References

Adelberger, K., et al. 2005, ApJ, 629, 636-653
Alexander, D., et al. 2005, ApJ, 632, 736-750

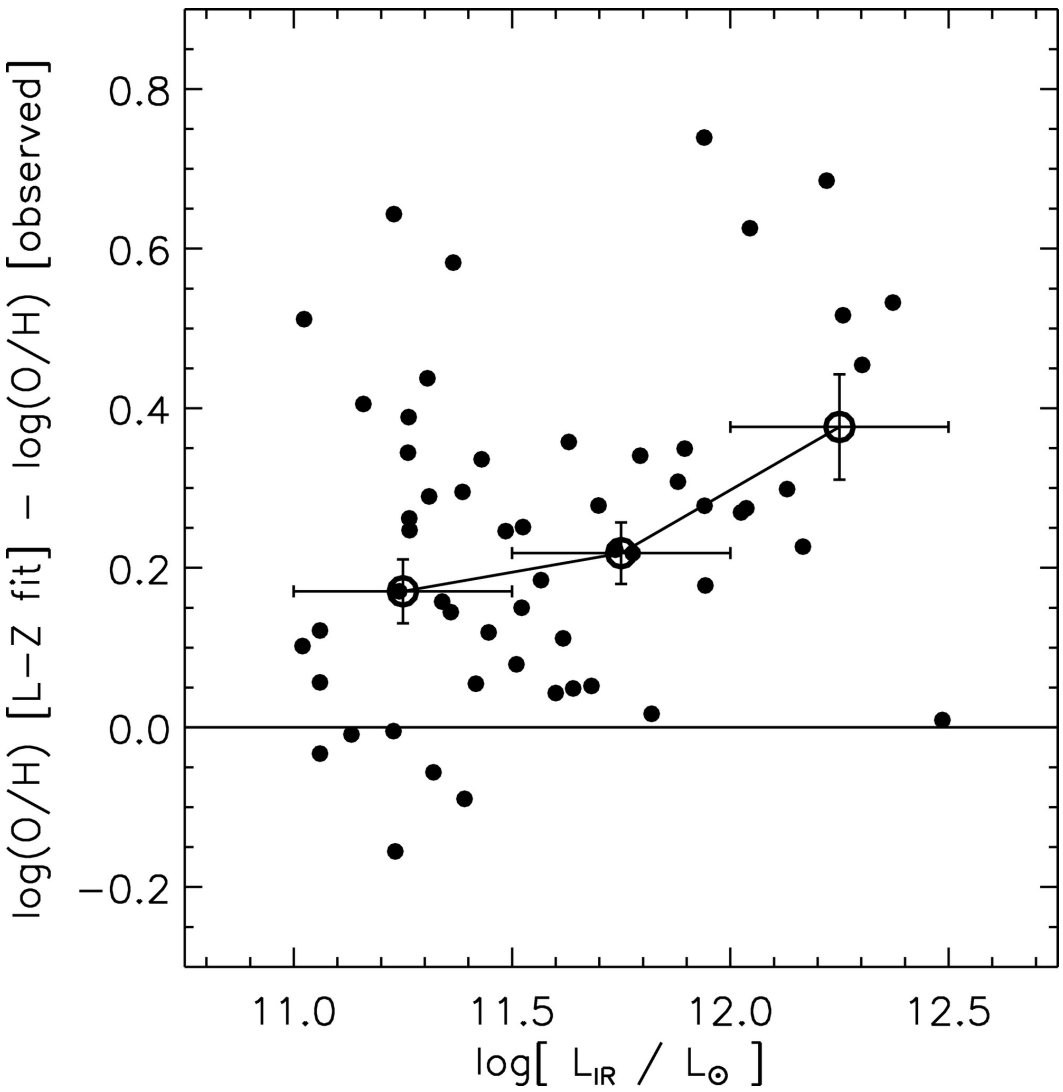

Fig. 27. Difference between the observed abundances in LIRGs and ULIRGs and the L-Z relation as a function of infrared luminosity. The small filled circles represent individual deviations from the L-Z relation. The thick open circles are median deviations from L-Z for equal-size bins centered on $\log[L_{IR}/L_{\odot}] = 11.25$, 11.75, and 12.25 and the error bars represent the standard error in the mean in each bin. LIRGs are offset by 0.2 dex, and ULIRGs by 0.4 dex. Comparison to the L-Z relation shows a mildly significant trend toward higher abundance offsets for higher L_{IR}. (From Rupke et al. 2008)

Alexander, D., et al. 2008, preprint. (astro-ph/0803.0634)
Bajtlik, S., Duncan, R. C., & Ostriker, J. P. 1988, ApJ, 327, 570-583
Begelman, M. C. 1985, ApJ, 297, 492-506
Binney, J., & Merrifield, M. 1998, Galactic Astronomy, Princeton, NJ: Princeton University Press, 796 p.
Binney, J., & Tremaine, S. 1987, Galactic Dynamics, Princeton, NJ: Princeton University Press, 747 p.
Blain, A., et al. 2002, PhR, 369, 111-176

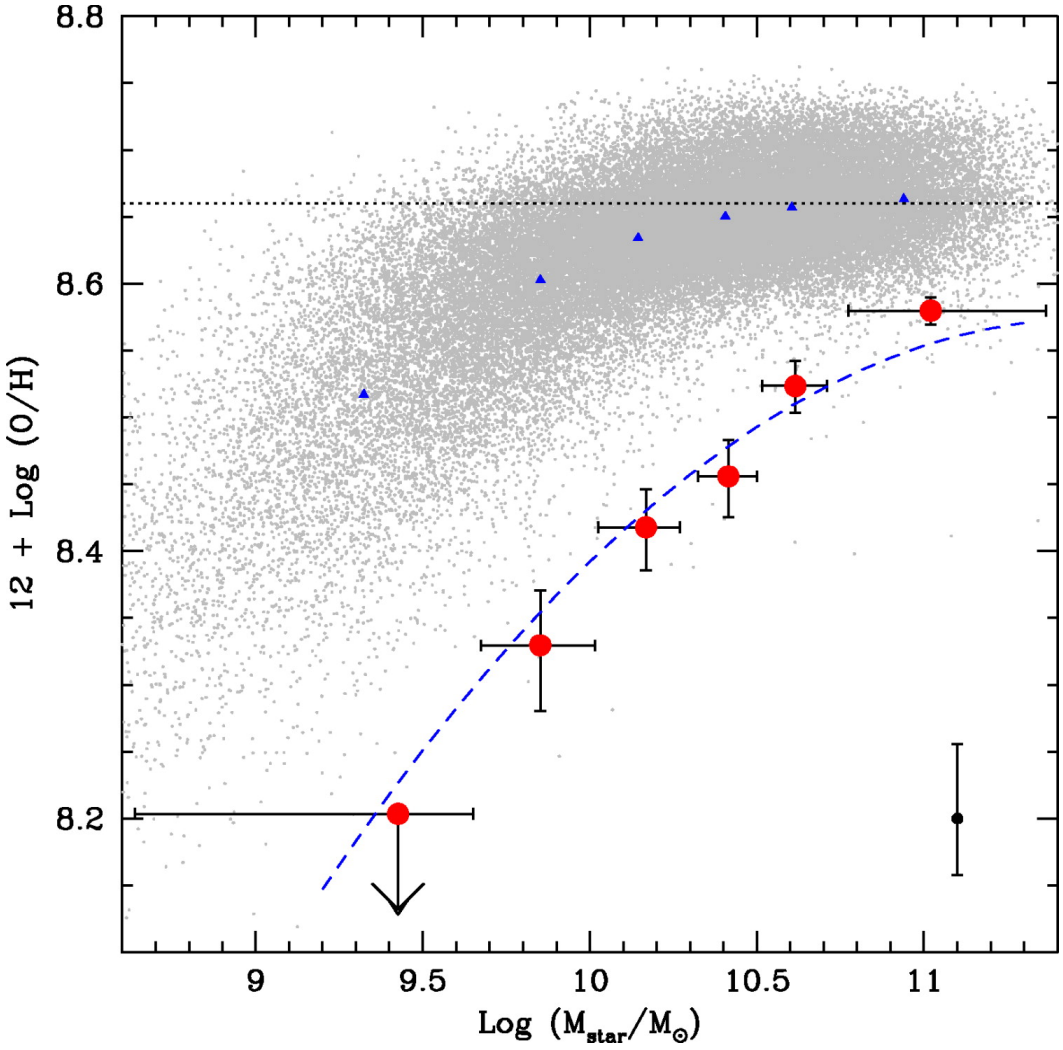

Fig. 28. Observed relation between stellar mass and oxygen abundance at $z \sim 2$, shown by the large red filled circles. Each point represents the average value of 14 or 15 galaxies, with the metallicity estimated from the [N II]/Hα ratio of their composite spectrum. Horizontal bars indicate the range of stellar masses in each bin, while the vertical error bars show the uncertainty in the [N II]/Hα ratio. The additional error bar in the lower right corner shows the additional uncertainty in the N2 calibration itself. The dashed blue line is the best-fit mass-metallicity relation of Tremonti et al. (2004), shifted downward by 0.56 dex. The metallicities of different samples are best compared using the same calibration; we therefore show, with small gray dots, the metallicities of the 53,000 SDSS galaxies of Tremonti et al. (2004) determined with the N2 index. Note that the [N II]/Hα ratio saturates near solar metallicity (horizontal dotted line). The blue filled triangles indicate the mean metallicity of the SDSS galaxies in the same mass bins as the high-z sample; using the more reliable, low-metallicity bins, the high-z galaxies are 0.3 dex lower in metallicity at a given mass. (From Erb et al. 2006)

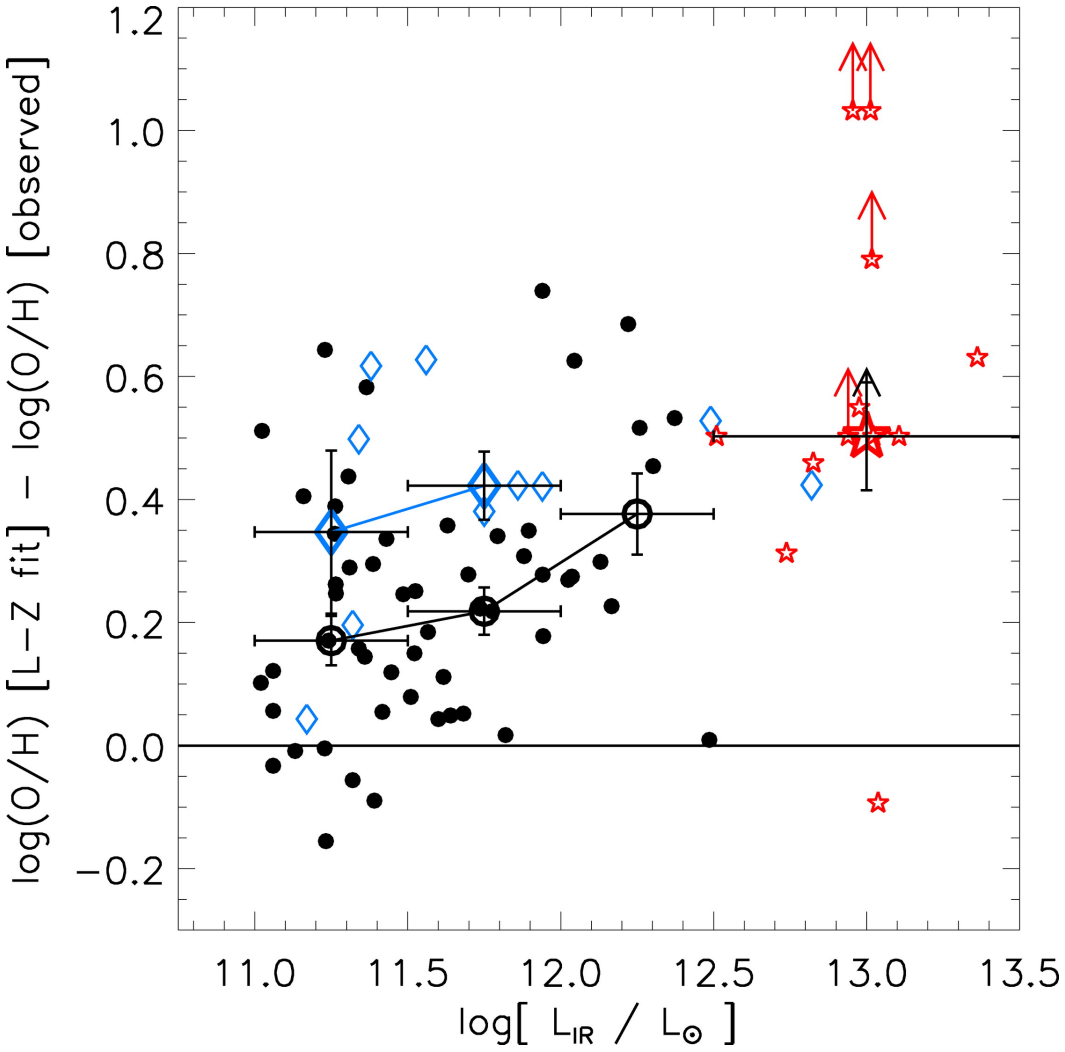

Fig. 29. Abundance offset from the local L-Z relation for low- and high-redshift LIRGs and ULIRGs, as a function of infrared luminosity. The black filled circles, blue open diamonds, and red open stars represent LIRGs and ULIRGs from Rupke et al. (2008), LIRGs and ULIRGs from Liang et al. (2004) and Rupke et al. (2008), and SMGs (Swinbank et al. 2004; Nesvadba et al. 2007), respectively. The black thick open circles, blue open diamonds, and open star are median deviations from L-Z for local LIRGs and ULIRGs, LIRGs, and SMGs, respectively. The LIRGs clearly evolve upward in abundance by 0.2 dex from $z \sim 0.6$ to $z \sim 0.1$, as would be expected from continual processing of heavy elements. Although there are only 2 ULIRGs in this figure, there is also apparent redshift evolution in ULIRG abundance from $z \sim 2$ to $z \sim 0.1$. Finally, there is also evidence for modest evolution from SMGs to ULIRGs, although the observed scatter and systematic uncertainties are large. (From Rupke et al. 2008)

Bland-Hawthorn, J., & Cohen, 2003. ApJ, 582, 246-256
Barnes, J. E., & Hernquist, L. 1996, ApJ, 471, 115-142
Borys, C., et al. 2005, ApJ, 635, 853-863
Castor, J., McCray, R., & Weaver, R. 1975, ApJ, 200, L107-L110

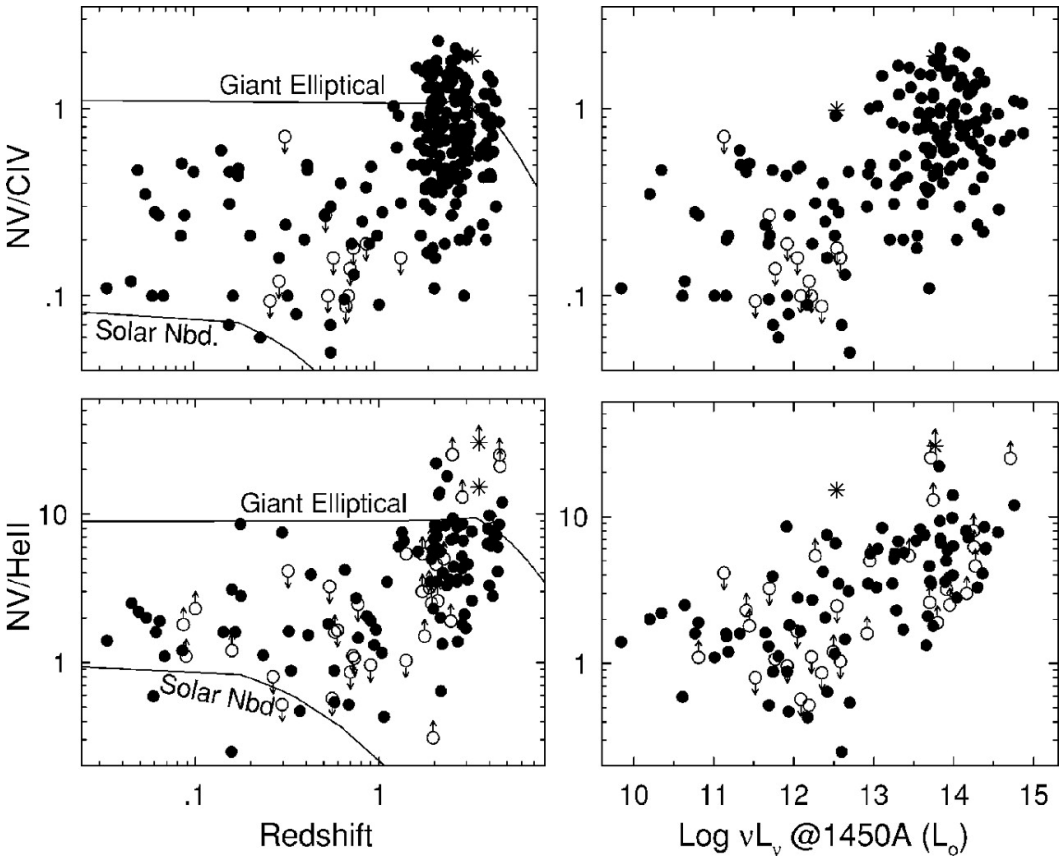

Fig. 30. Measured NV/HeII and NV/CIV flux ratios versus redshift (left panels) and continuum luminosity (right). The upper and lower ranges might be undersampled (especially for NV/HeII at redshifts > 1) because limits on weak lines (e.g. HeII) were often not available from the literature. The two asterisks in each panel represent mean values measured by Osmer, Porter, & Green (1994) for high- and low-luminosity QSOs at redshift >3. The solid curves are predictions based on chemical evolution models. (From Hamann & Ferland 1999)

Cecil, G., et al. 2001, ApJ, 555, 338-355
Cecil, G., Bland-Hawthorn, J., & Veilleux, S. 2002, ApJ, 576, 745-752
Chapman, S. C., et al. 2003, ApJ, 599, 92-104
Chapman, S. C., et al. 2004, ApJ, 611, 732-738
Chapman, S. C., et al. 2005, ApJ, 622, 772-796
Cid Fernandes, R., et al. 2004, MNRAS, 355, 273-296
Cid Fernandes, R. Jr. & Terlevich, R. 1995, MNRAS, 272, 423-441
Dasyra, K., et al. 2006a, ApJ, 638, 745-758
Dasyra, K., et al. 2006b, ApJ, 651, 835-852
Dasyra, K., et al. 2007, ApJ, 657, 102-115
Devine, D., & Bally J. 1999, ApJ, 510, 197-204
Downes, D., & Solomon, P. M. 1998, ApJ, 507, 615-654
Edmunds, M. G., & Pagel, B. E. J. 1984, MNRAS, 211, 507-519
Engelbracht, C. W., et al. 2006, ApJ, 642, L127-L132
Erb, D. K., et al. 2006, ApJ, 644, 813-828

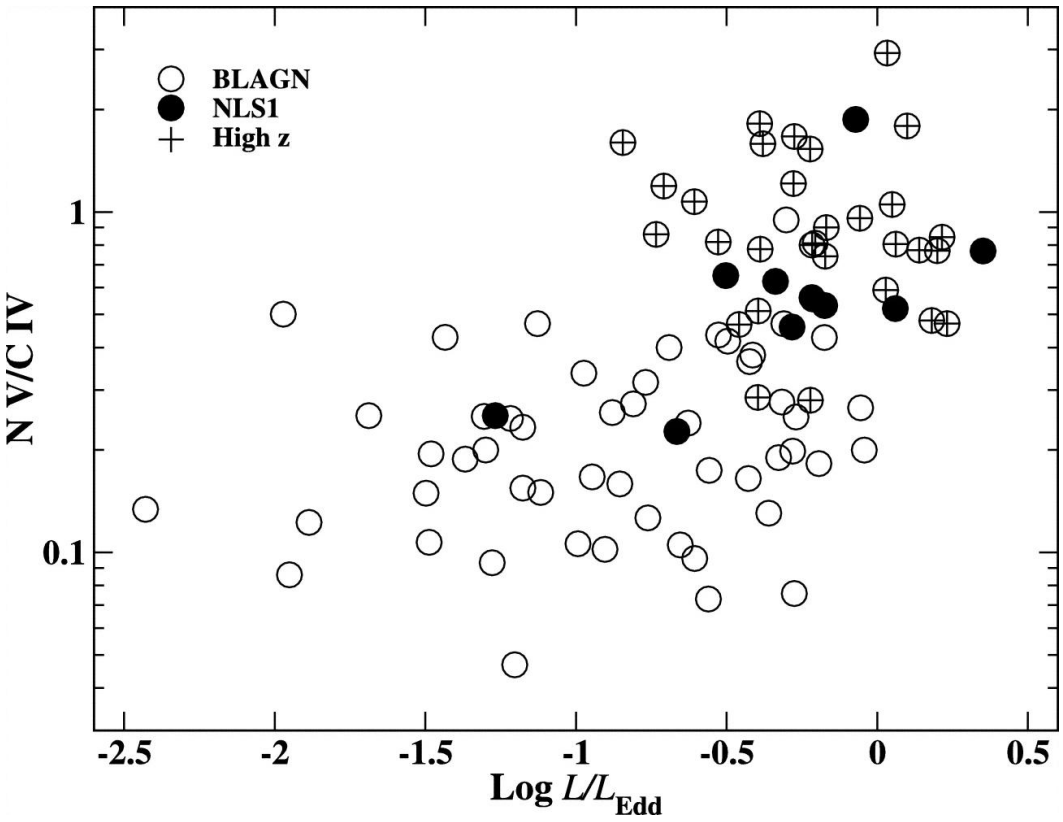

Fig. 31. N V/C IV vs. accretion rate. A strong metallicity-accretion rate correlation for all AGNs is apparent, and most NLS1s are found in the same region of parameter space that is shared by the high-z quasars. Note that the location of Mrk 766 (the NLS1 with the lowest accretion rate in this diagram) may be affected by strong intrinsic reddening (from Shemmer et al. 1994).

Evans, A. S., et al. 2001, AJ, 121, 1893-1902
Ferrara, A. 2007, EAS Publications Series, Vol. 24, pp. 229-243
Ferrarese, L., & Merritt, D. 2000, ApJ, 539, L9-L12
Fukugita, M., Hogan, C. J., & Peebles, P. J. E. 1998, ApJ, 503, 518-530
Garnett, D. R. 2002, ApJ, 581, 1019-1031
Gebhardt, K., et al. 2000, ApJ, 539, L13-L16
Genzel, R., et al. 2001, ApJ, 563, 527-545
González Delgado, R. M., et al. 1998, ApJ, 495, 698-717
González Delgado, R. M., Heckman, T., & Leitherer, C. 2001, ApJ, 546, 845-865
Griffiths, R. E., et al. 2000, Sci, 290, 1325-1328
Hamann, F., & Ferland, G. 1999, ARA&A, 37, 487-531
Heckman, T. M., et al. 1997 ApJ, 482, 114-132
Hoopes, C. G., et al. 2005, ApJ, 619, L99-L102
Hopkins, P. F., et al. 2006, ApJS, 163, 1-49
Ishida, K. 2004, PhD Thesis, University of Hawaii
Joguet, B., A&A, 380, 19-30
Kauffmann, G., et al. 2003a, MNRAS, 341, 54-69

Kauffmann, G., et al. 2003b, MNRAS, 346, 1055-1077
Kennicutt, R. C. Jr., Bresolin, F., & Garnett, D. R. 2003, apJ, 591, 801-820
Kennicutt, R. C. Jr. 1998, ARAA, 36, 189-231
Kewley, L. J., et al. 2001, ApJ, 556, 121-140
Kewley, L. J., & Dopita, M. A. 2002, ApJS, 142, 35-52
Kobulnicky, H. A., & Kewley, L. J. 2004, ApJ, 617, 240-261
Kormendy, J., & Djorgovski, S. 1989, ARA&A, 27, 235-277
Le Floc'h, E., et al. 2005, ApJ, 632, 169-190
Lehnert, M. et al. 1999, ApJ, 523, 575-584
Liang, Y. C., et al. 2004, A&A, 423, 867-880
Lonsdale, Farrah, & Smith 2006, Astrophysics Update 2, edited by John W. Mason, p. 285
Lutz, D., Veilleux, S., & Genzel, R. 1999, ApJ, 517, L13-L17
Maiolino, R., et al. 2007a, A&A, 468, 979-992
Maiolino, R., et al. 2007b, A&A, 472, L33-L37
Martin, C., Kobulnicky, H. A., & Heckman, T. M. 2002, ApJ, 574, 663-692
Matsushita, S., et al. 2004, The Neutral ISM in Starburst Galaxies, ASP Vol. 320, eds. S. Aalto, S. Huttemeister, and A. Pedlar, p. 138
McGaugh, S. S. 1991, ApJ, 380, 140-150
Mihos, J. C., & Hernquist, L. 1996, ApJ, 464, 641-663
Muñoz Marín, et al. 2007, AJ, 134, 648-667
Murray, N., Quataert, E., & Thompson, T. A. 2005, ApJ, 618, 569-585
Nesvadba, N. P. H., et al. 2007, ApJ, 657, 725-737
Netzer, H., et al. 2007, ApJ, 666, 806-816
Nordstrom, Andersen, & Mayor 2005, in The Three-Dimensional Universe with Gaia, eds. C. Turon, K. S. O'Flaherty, M.A.C. Perryman, 183-186
Osmer, P. S., Porter, A. C., & Green, R. F. 1994, ApJ, 436, 678-695
Osterbrock, D. E., Tran, H., & Veilleux, S. 1992, ApJ, 389, 196-207
Rich, M. R. 1990, ApJ, 362, 604-619
Riffer, R., et al. 2007, ApJ, 659, L103-L106
Robert, C., Leitherer, C., & Heckman, T. M. 1993, ApJ, 418, 749-759
Rupke, D. S. R., Veilleux, S., & Baker, A. J. 2008, ApJ, 674, 172-193
Rupke, D. S. N., Veilleux, S., & Sanders, D. B. 2005a, ApJS, 160, 87-115
Rupke, D. S. N., Veilleux, S., & Sanders, D. B. 2005b, ApJS, 160, 115-148
Rupke, D. S. N., Veilleux, S., & Sanders, D. B. 2005c, ApJ, 632, 751-780
Salzer, J. J., et al. 2005, ApJ, 624, 661-679
Sanders, D. B., & Mirabel, I. F. 1996, ARA&A, 34, 749-792
Sanders, D. B., et al. 1988a, ApJ, 325, 74-91
Sanders, D. B., et al. 1988b, ApJ, 328, L35-L39
Sanders, D. B., et al. 1988c, ApJ, 324, L55-L58
Savaglio, S., et al. 2005, ApJ, 635, 260-279
Schwartz, C. M., & Martin, C. L. 2004, ApJ, 610, 201-212
Schweitzer, M., et al. 2006, ApJ, 649, 79-90
Sedov, L. I. 1959, Similarity and Dimensional Methods in Mechanics, New York: Academic Press

Shapley, A. E., et al. 2003, ApJ, 588, 65-89
Shemmer, O., et al. 2004, ApJ, 614, 547-5578
Shi, Y., et al. 2007, ApJ, 669, 841-861
Shopbell, P. L., & Bland-Hawthorn, J. 1998, ApJ, 493, 129-153
Silk, J. 2003, MNRAS, 343, 249-254
Smail, I., et al. 2002, MNRAS, 331, 495-520
Smail, I., et al. 2004, ApJ, 616, 71-85
Sofue, Y., & Handa, T. 1984, Nature, 310, 568-569
Soifer, B. T., et al. 2000, AJ, 119, 509-523
Stevens, I. R., Read, A. M., & Bravo-Guerrero, J. 2003, MNRAS, 343, L47-L52
Swinbank, A. M., et al. 2004, ApJ, 617, 64-80
Tacconi, L. J., et al. 2002, ApJ, 580, 73-87
Taylor, G. 1950, Proc. R. Soc. London Ser. A 2001, 159
Terlevich, E., Diaz, A. I., & Terlevich, R. 1990, MNRAS, 242, 271-284
Tinsley, B. M. 1980, Fund. of Cosmic Physics, 5, 287-388
Tran, Q. D., et al. 2001, ApJ, 552, 527-543
Tremonti, C. A., et al. 2004, ApJ, 613, 898-913
Veilleux, S. 2001, in Starburst Galaxies: Near and Far, ed. L. Tacconi & D. Lutz (Heidelberg: Springer), 88-95
Veilleux, S., Cecil, C., & Bland-Hawthorn, J. 2005, ARA&A, 43, 769-826
Veilleux, S., Kim, D. C., & Sanders, D. B. 1999, ApJ, 522, 113-138
Veilleux, S., Kim, D. C., & Sanders, D. B. 2002, ApJS, 143, 315-376
Veilleux, S., & Osterbrock, D. E. 1987, ApJS, 63, 295-310
Veilleux, S., Sanders, D. B., & Kim, D. C. 1999 , ApJ, 522, 139-156
Veilleux, S., et al. 1994, ApJ, 433, 48-64
Veilleux, S., et al. 1995, ApJS, 98, 171-217
Veilleux, S., et al. 2003, AJ, 126, 2185-2208
Veilleux, S., et al. 2006, ApJ, 643, 707-723
Veilleux, S., et al. 2008, in prep.
Walter, F., Weiss, A., & Scoville, N. 2002, ApJ, 580, L21-L25
Weaver, R., et al. 1977, ApJ, 218, 377-395
Wilson, A. S., & Tsvetanov, Z. 1994, AJ, 107, 1227-1234
Wisotzki, L. 2000, A&A, 353, 853-860
Yuasa, T., et al. 2007, preprint, astro-ph/0709.1580
Zaritsky, D., Kennicutt, R. C. Jr., & Huchra, J. P. 1994, ApJ, 420, 87-109